A model of suboxic sedimentary diagenesis suitable for automatic tuning and gridded global domains

D. E. Archer
Department of Geophysical Science, University of Chicago, Chicago, Illinois, USA

J. L. Morford
Woods Hole Oceanographic Institution, Woods Hole, Massachusetts, USA

S. R. Emerson
School of Oceanography, University of Washington, Seattle, Washington, USA

Received 11 April 2000; revised 24 May 2001; accepted 22 June 2001; published 30 March 2002.

[1] We present a new model for oxic and anoxic diagenesis of shallow and deep-sea sediments based on an efficient solver for steady state pore water and solid phase diffusion/reaction/advection equations. The model, called "Muds", is orders of magnitude faster than solvers of the corresponding time-dependent equations. The model resolves Mn and Fe/S geochemistry as well as pore water pH and $CaCO_3$ dissolution. The model speed opens application possibilities that are impossible for time-dependent models, including automatic tuning of uncertain parameters, and deployment of the model in gridded global domains. The kinetic rate constants for respiration and bioturbation are parameterized as functions of the organic carbon rain to the seafloor, based on existing parameterizations in the literature. Seven uncertain model parameters, including many of the rate constant parameterizations, were tuned to minimize the misfit to observations from 53 sedimentary locations throughout the ocean. The model tuning knobs were the fractions of labile and refractory organic matter in the sedimenting material, the NO_3^-, Mn, Fe, and S respiration rate constant parameterizations, and the depth scales of respiration and of pore water irrigation. We searched for adequate fit values of these parameterizations using a simulated annealing method. The cost function (degree of misfit) was based on a comparison of pore water (NO_3^-, NH_4^+, Mn^{2+}, and Fe^{2+}) and solid phase (organic carbon and MnO_2) model results with data. Many of the tuning parameters are constrained to ±50% or better. The model is most skillful at predicting organic carbon concentration, depth of NO_3^- penetration, and pore water Fe^{2+}, and less so for Mn^{2+}, NH_4^+, and solid phase MnO_2. The model misses some of the very high sediment surface MnO_2 concentrations observed in, for example, the California Borderlands. We believe that these sites must receive a higher input of reactive Mn than the crustal abundance of the clay rain. The model was deployed on every $2° \times 2°$ grid point below 1000 m of the global seafloor, using gridded maps of organic carbon rain to the seafloor and overlying water chemistry. The deep-sea carbon burial efficiency is 7%, with 95% of respiration by oxic metabolism. The model was also run against a new depth-oxygen hypsometry of the global ocean, with sediment area as a function of overlying oxygen concentration and average depth related to carbon fluxes, to include the effects of shallow water sediments. This analysis predicts that shallow waters (<1000 m) account for 88% of respiration, and oxygen accounts for 66% of respiration overall. Denitrification is closely coupled to organic nitrogen fluxes to the sediment, and the global rate is estimated to be 1.4×10^{14} mol yr^{-1}, a factor of 6–8 higher than the corresponding estimate from *Middelburg et al.* [1996], throwing the nitrogen cycle in the ocean into imbalance. *INDEX TERMS:* 4863 Oceanography: Biological and Chemical: Sedimentation; 4851 Oceanography: Biological and Chemical: Oxidation/reduction reactions; 4804 Oceanography: Biological and Chemical: Benthic processes/benthos; 4805 Oceanography: Biological and Chemical: Biogeochemical cycles (1615); *KEYWORDS:* diagenesis

1. Introduction

[2] Oxidation/reduction chemistry of sediment is an integral part of the global carbon cycle, serving both as an indicator and as a player in processes that affect the pCO_2 of the atmosphere. Many proposals for lowering pCO_2 during glacial time invoke a more vigorous biological pump [*Archer and Maier-Reimer*, 1994; *Archer et al.*, 2000; *Broecker and Henderson*, 1998; *Knox and McElroy*, 1984; *Sarmiento and Toggweiler*, 1984; *Siegenthaler and Wenk*, 1984], stimulated perhaps by an increase in iron deposition to the ocean surface [*Mahowald et al.*, 1999; *Martin and Fitzwater*, 1988; *Peteet et al.*, 1990] or an increase in the global ocean inventory of NO_3^- [*Broecker and Henderson*, 1998; *McElroy*, 1983].

Copyright 2002 by the American Geophysical Union.
0886-6236/02/2000GB001288$12.00

Table 1. Sedimentary Model Reactions and Rate Expressions

Reaction	First Order	Zero Order
$OrgC^a + 138\ O_2 \rightarrow 106\ CO_2 + 16\ NO_3^-$	OrgC	
$Mn^{2+} + 1/2\ O_2 + H_2O \rightarrow MnO_2 + 2\ H^+$	Mn^{2+}	O_2
$OrgC + 236\ MnO_2 + 472\ H^+ \rightarrow 236\,Mn^{2+} + 106\,CO2 + 16\,NO_3^-$	OrgC	$-O_2, +MnO_2$
$OrgC + 94.4\ HNO_3 \rightarrow 106\ CO_2 + 47.2\ N_2$	OrgC	$-O_2, +NO_3^-$
$5 \cdot Fe^{2+} + NO_3^- \rightarrow FeOOH + N_2 + 9H^+$	Fe^{2+}	$+NO_3^-$
$OrgC + 472\ FeOOH + 960\ H^+ \rightarrow 106\ CO_2 + 472\ Fe^{2+} + 16\,NH_4^+$	OrgC	$-NO_3^-$
$OrgC + 59\ SO_4^{2-} + 75H^+ \rightarrow 106\ CO_2 + 16\,NH_4^+ + 59\ HS^-$	OrgC	$-NO_3^-$
$HS^- + 2\ O_2 \rightarrow SO_4^{2-} + H^+$	HS^-	$+ O_2$
$HS^- + Fe^{2+} \rightarrow FeS + H^+$	HS^-, Fe^{2+}	
$FeS + 4.5\ O_2 + H^+ \rightarrow FeOOH + SO_4^{2-}$	FeS	$+ O_2$
$CaCO_3 \rightarrow Ca^{2+} + CO_3^-$	$1 - \left[CO_3^=\right] \Big/ \left[CO_3^=\right]_{sat}$	
$SiO_2 \rightarrow H_4SiO_4$	$[SiO_2]$, $\Delta[H_4SiO_4]$	

[a] OrgC is Redfield organic matter, $(CH_2O)_{106}(NH_3)_{16}$.

[3] The biological pump may further affect atmospheric pCO_2 indirectly by the mechanism of $CaCO_3$ compensation, which controls the pH of the ocean [*Archer and Maier-Reimer*, 1994; *Archer et al.*, 2000; *Broecker and Peng*, 1987]. Oxic organic carbon respiration in sediments liberates carbon in the form of dissolved CO_2, acidifying the pore water and provoking the dissolution of $CaCO_3$ [*Emerson and Bender*, 1981]. The effect of suboxic and anaerobic respiration on pore water pH is more complicated than for oxic respiration, but in general, these reactions have the opposite (and perhaps a smaller) effect on pH and therefore $CaCO_3$ preservation than oxic respiration [*Berner et al.*, 1970; *Canfield*, 1989]. The dominant suboxic electron acceptor in the redox conditions of the abyss, for example, is NO_3^-, which produces mostly HCO_3^-. Models of the pCO_2 response to the strength of the biological pump must therefore consider the preservation of $CaCO_3$ as a function of sediment redox chemistry [*Archer et al.*, 2000].

[4] Sinking organic matter carries with it an associated oxygen demand, such that an increase in biological sequestration of CO_2 in the deep sea will be associated with a corresponding decrease in deep-sea oxygen [*Sarmiento and Orr*, 1991]. The oxygen concentration beneath the sediment surface, recorded by sedimentary redox tracers, is determined by two factors, both of which can be affected by changes in the strength of the biological pump. One is the overlying water oxygen concentration, serving as the upper boundary condition for sedimentary diagenesis. The other is consumption within the sediment, determined by the balance between the downward fluxes of organic carbon vs. dissolved oxygen.

[5] Many sedimentary redox tracers, such as manganese, organic carbon, and trace metals, cycle through geologic time, often correlated with global climate [*Berger et al.*, 1983; *Calvert and Padersen*, 1993; *Crusius et al.*, 1996; *Dean et al.*, 1994, 1997; *Francois*, 1993; *Nameroff*, 1996; *Rosenthal et al.*, 1995]. The problem which invariably plagues studies of paleo-sediment redox state is quantitative interpretation: Was the change in sediment chemistry caused by organic carbon rain to the seafloor, overlying water oxygen concentration, or both? For example, high concentrations of authigenic uranium found in Southern Ocean sediments might indicate either a stronger Southern Ocean biological pump [*Anderson et al.*, 1998] or a poorly ventilated Southern Ocean [*Francois et al.*, 1998]. *Morford and Emerson* [1999] argue, based on global metal mass balances and V and Cd concentrations observed in foraminifera, that the area of reducing sediments, where O_2 penetrates <1 cm, cannot have more than doubled in the past 40,000 years. Again, however, their constraint reflects a combination of organic carbon rain and deep-sea oxygen concentration.

[6] We present a new sediment redox diagenesis model called Muds (just a name, not an acronym). Muds belongs to an efficient class of sediment diagenesis models which use relaxation methods to iterate to steady state solutions [*Archer et al.*, 1993; *Archer*, 1991; *Martin and Sayles*, 1990; *Soetaert et al.*, 1996]. These methods reach the steady state orders of magnitude faster than time-dependent models can. Muds takes less than a minute to solve for pore water and solid phase steady state in the upper meter of the sediment. It is possible to use relaxation models in ways which are more difficult for time-dependent models, such as automatic tuning [*Soetaert et al.*, 1996] and application to large gridded global domains [*Archer*, 1996b; *Archer et al.*, 2000]. Muds is the first of this class of models to resolve the suboxic manganese, iron, and sulfur redox systems. Pore water constituents include O_2, NO_3^-, Mn^{2+}, Fe^{2+}, $NH_4^=$, $CO_3^=$, and H_4SIO_4, and the solid phase includes two phases of organic carbon, MnO_2, FeOOH, $CaCO_3$, and SiO_2. The behavior of redox trace metals such as authigenic UO_2 within Muds is described by *Morford* [1999] and will be published separately.

[7] The rate constants for biologically mediated processes such as respiration and bioturbation are site-specific in the real ocean, generally correlated with overall sediment respiration or accumulation rate. We have attempted to generalize the model by parameterizing many of these rate constants as functions of the sediment respiration rate. These parameterization functions are tuned using automatic methods to minimize the misfit to a data set from 53 locations throughout the Atlantic and Pacific slope and abyss. Using these tuned parameterizations, we drive the model with gridded seafloor data (as *Archer* [1996b]) and predict global respiration and burial rates.

2. Model Formulation

2.1. Description

[8] The Muds model is based on the steady state diffusion-reaction equations for pore water and solid sediment. The model equations and reaction kinetics are similar to previously published sedimentary diagenetic models [*Archer*, 1991; *Burdige and Geiskes*, 1983; *van Cappellen and Wang*, 1996] and are given in Table 1. Two types of organic carbon rain to the seafloor and react initially with O_2 in the pore waters [*Berner*, 1980]. NO_3^- serves as an electron acceptor below the depth where O_2 is depleted. In this zone, solid MnO_2 is also used as an electron

acceptor for respiration, producing dissolved Mn^{2+}, which can precipitate to MnO_2 in the oxic zone or $MnCO_3$ at depth. Below the depth where NO_3^- is depleted, SO_4^{2-} and solid FeOOH are used as electron acceptors, producing dissolved Fe^{2+} and HS^-, which can either precipitate as FeS or diffuse to the oxic zone. Bioturbation can also expose solid FeS to oxidation. Irrigation of the pore water is simulated as a depth-dependent exchange with the overlying water, with an exchange rate parameterized as a function of organic carbon rain. Surface-active species such as Fe^{2+}, Mn^{2+}, NH_4^+, and H^+ can be adsorbed onto solid phases and transported by bioturbation or advection. Other solid phases include $CaCO_3$ and SiO_2, which dissolve using first-order dissolution kinetics, and nonreactive clay. The model does not currently simulate time-dependent behavior, such as the generation of relict manganese layers [*Berger et al.*, 1983; *Schmitz et al.*, 1999].

2.2. Differential Equations

[9] The equation for a pore water solute concentration c is

$$\phi\frac{\partial c}{\partial t} = 0 = \frac{\partial}{\partial z}\left(\frac{D_c}{F}\frac{\partial c}{\partial z}\right) + I_z(c_0 - c) + \frac{\partial}{\partial z}\left(D_B\frac{\partial c_{ads}}{\partial z}\right) - \Omega\frac{\partial c_{ads}}{\partial z} - J_c, \quad (1)$$

where ϕ is porosity, D_c is the diffusion coefficient for solute c, F is the formation factor of the sediment (how much the solid matrix slows down diffusion), and z is depth (positive downward). I_z is a depth-dependent irrigation coefficient with units of inverse time. Adsorbed solute c_{ads}, assuming equilibrium, is transported by bioturbation (using solid mixing rate D_B) and burial O; the divergence of c_{ads} is treated as a source or sink for c. J_c is the reaction rate, described below. The solid species are governed by the equation

$$(1-\phi)\frac{\partial \%S}{\partial t} = 0 = \frac{\partial}{\partial z}\left[D_B(1-\phi)\frac{\partial \%S}{\partial z}\right] - \Omega\frac{\partial \%S}{\partial z} - J_S, \quad (2)$$

where the units of the solid concentration S, is g g^{-1} dry weight. D_B is the depth-dependent solid diffusion (bioturbation) rate, and Ω is the rate of sediment burial. In both types of equation the time-dependent terms equal zero, indicating that we seek the steady state profiles of all solid and pore water constituents. The top boundary condition for solutes is the overlying water concentration, and for solids, the sediment rain rate. A condition of no gradient is imposed at the bottom boundary for all constituents.

2.3. Discrete Equations

[10] The model is discretized on a 17-depth grid. The cell thickness ranges from 0.05 cm at the sediment surface to 35 cm in the deepest box, reaching a depth (z) span of 100 cm. (In the discretized diffusion equation, the diffusive flux of oxygen can be no greater than

$$\mathrm{Flux}_{max} = D\frac{\partial O_2}{\partial z} = D\frac{O_{2_{\mathrm{bottom\ water}}}}{\Delta z_{top}} \quad (3)$$

Thus Δz_{top}, the thickness of the top box, sets an upper limit on the diffusive flux of oxygen across the sediment-water interface. Fine grid spacing is desirable, but in time-dependent models, Δz limits the time step, making detail in this region expensive to resolve. The relaxation method faces no such restriction.) Concentrations are defined in the box centers, burial rates at the cell bottoms. The model seeks the condition where fluxes across the cell boundaries are balanced against reaction rates within each box.

[11] The model consists of a series of depth-dependent difference equations. These equations, one for each chemical species in the pore water or solid phase, are tightly and nonlinearly coupled to each other by dissolution or precipitation reaction rates (for example, there is coupling between O_2 and organic carbon). In addition, the solid phases are all indirectly coupled to each other by solid phase advection, which is determined by the sum of the dissolution reaction rates, all of which depend in nonlinear ways on solid and solute concentrations. We attack this tangled mess of equations by successive approximation using a gradient-descent (Newton's) method.

[12] One possible approach (which would be interesting to try as it might be faster) would be to simultaneously relax all concentration values at all depths (a linear algebra problem of $n_z \times n_{solvents} \times n_{solutes}$ equations, in our case 3,332). We chose instead the strategy of separating the systems numerically wherever possible. The iteration proceeds in stages; first each pore water profile is iterated to steady state given the current guess for the solid phase profiles. Then the solid phase profiles are iterated a few times using the new reaction rates calculated from the pore water chemistry. For the systems $Mn^{2+}/MnO_2/MnCO_3$ and $FeOOH/Fe^{2+}/HS^-/FeS$, special steps had to be taken to reach solution; these will be described below.

[13] For a solute c_i in box i, the model calculates the imbalance in the fluxes of the species (R_i) as

$$R_i = \frac{D_M}{\phi_i\Delta z_i}\left(\frac{F_{i+1}+F_i}{\Delta z_{i+1}+\Delta z_i}(c_{i+1}-c_i) - \frac{F_i+F_{i-1}}{\Delta z_{i+1}+\Delta z_i}(c_i-c_{i-1})\right) + \frac{D_{B_{i+1}}}{\Delta z_i}\frac{2}{\Delta z_{i+1}+\Delta z_i}\left(c_{ads_{i+1}}-c_{ads_i}\right) - \frac{D_{B_{i-1}}}{\Delta z_i}\frac{2}{\Delta z_{i-1}+\Delta z_i}(c_{ads_i}-c_{ads_{i-1}}) - (\Omega_{i-1}c_{ads_{i-1}}-\Omega_i c_{ads_i})\frac{\Phi_i\rho_{solid}}{(1-\Phi_i)\Delta z_i} + I_z(c_0-c_i) + J_i \quad (4)$$

where D_{Bi} and Ω_l are defined at the bottom of box i, ρ_{solid} is the dry density of solid material (2.5 g cm^{-3}), and everything else is as defined above. For a solid, the residual R_i is calculated

$$R_i = \frac{1}{\Delta z_i(1-\Phi_i)}\left(D_{B_{i+1}}\frac{2(2-\Phi_{i+1}-\Phi_i)}{\Delta z_{i+1}+\Delta z_i}(S_{i+1}-S_i) - D_{B_i}\cdot\frac{2(2-\Phi_i-\Phi_{i-1})}{\Delta z_i+\Delta z_{i-1}}(S_i-S_{i-1}) + \frac{\Omega_{i-1}}{\rho_{solid}}S_{i-1} - \frac{\Omega_i}{\rho_{solid}}S_i + J_i\right) \quad (5)$$

[14] The steady state solution is where all $R_i = 0$ for all species at all depths. The next guesses for each c_i and s_i are determined by a gradient-descent, or Newton's, method for finding the zero to a function. For an analogous one-dimensional system, we seek x such that $f(x) = 0$. From an initial guess x we compute the next guess, $x + \Delta x$, as the zero intercept of the tangent to $f(x_1)$

$$\Delta x = -f(x_1)\left(\left.\frac{\partial f}{\partial x}\right|_{x_1}\right)^{-1}. \quad (6)$$

In the multidimensional system, n equations representing n boxes are solved simultaneously,

$$\mathbf{J}(R,c)\cdot\Delta\mathbf{x} = -\mathbf{R}, \quad (7)$$

where the Jacobian $\mathbf{J}$ is a matrix of $\partial R_i/\partial c_j$ and $\Delta\mathbf{x}$ and $\mathbf{R}$ are vectors over all grid boxes i. The boundary conditions are built into the system of equations by modifying R_i in the sediment surface and deepest boxes to include diffusive flux or sediment rain at the top or zero diffusive flux at the bottom.

2.4. Treatment of Monod Kinetics

[15] Several chemical systems within the model are treated with zero-order "Monod" kinetics, where the reaction rate is independent of substrate concentration (zero order) as long as the concentration exceeds some critical value, but the reaction is forbidden when the reactant drops below that value [*Devol*, 1978; *Postma and Jakobsen*, 1996]. Taking oxygen as an example, in oxygenated sediments the consumption rate is

$$J = k[\mathrm{OrgC}], \tag{8}$$

but oxygen consumption ceases in anaerobic sediments. The rate constant k is therefore discontinuous across the anoxic boundary. We solve this type of system by iterating in this example z_{oxic}, the depth of oxygen penetration, to generate a reasonable oxygen profile. The rate within a grid box is proportional to the depth fraction of the box that is above the depth of oxygen penetration z_{oxic} (implicitly assuming that organic carbon is well mixed within the box). The correct value for z_{oxic} produces the physically realistic solution with a nonnegative concentration and zero flux at the bottom boundary z_{max}. If the current guess for z_{oxic} is too deep, the no-flux condition requires a negative concentration at z_{max}. The next guess for z_{oxic} should be shallower. In oxygen-unlimited conditions the correct solution is $z_{\mathrm{oxic}} = z_{\mathrm{max}}$. Similar tests and strategies are employed for the penetration depth of NO_3^-, MnO_2, and FeOOH.

2.5. Solute Adsorption

[16] Steady state concentration profiles of several of the solutes need to be adjusted for adsorption onto solid surfaces. Adsorption may dominate the inventories of the surface active solutes in Muds: Fe^{2+}, Mn^{2+}, NH_4, and H^+. However, in the steady state the salient comparison is not between the concentrations but rather between the vertical fluxes of adsorbed versus pore water solute. In the limit of no solid phase transport, where the only way to move Fe^{2+}, for example, is to diffuse it within the pore water, the pore waters will relax to the same concentration profile in the steady state regardless of adsorption. Adsorption alters the steady state pore water concentrations only insofar as vertical mixing or advection of the solid phase acts as a source or sink of solute. Given a current guess for the concentration of solute in the pore water, the model calculates the concentration of adsorbed species assuming equilibrium, c_{ads} in (4), following *Wang and van Cappellen* [1996]. The vertical fluxes are then computed from the adsorbed concentration profile and the solid phase mixing and burial (advection) rates. Similarly, dissolved boron and protons diffuse in the pore waters, generating a source for alkalinity in the carbon chemistry routine (based on *Archer* [1991]).

2.6. Pore Water Irrigation

[17] In shallow-water sediments it is observed that solute transport to the overlying water is enhanced by the action of benthic animals [*Aller*, 1980; *Archer and Devol*, 1992; *Jorgensen and Revsbech*, 1985]. We simulate this process as a nonlocal fluid exchange between pore and overlying waters [*Boudreau*, 1984; *Emerson et al.*, 1984]. The highly reactive solutes Fe^{2+} and Mn^{2+} are assumed to oxidize to their solid forms, either at depth in the sediment or at the sediment surface, depending on the relative concentrations of oxidizers in the overlying water and reductants in the pore water, rather than escaping to the overlying water in dissolved form.

2.7. Solute/Solid Coupling

[18] The reaction rates of the solid phases depend heavily on the pore water chemistry, for example, oxic respiration depends on z_{oxic}, and calcite dissolution depends on $CO_3^=$. The model iteration scheme alternates between the solute and solid phase systems, seeking a coupled solution to both. Within each cycle the solute profiles are relaxed completely to steady state, based on the current guess of the solid phase concentrations. Then the solid phases undergo 10 relaxation passes using the reaction rates calculated from the solute system before returning to the solute routines. The solute and solid systems are coupled using a reaction rate "mail trolley" scheme which carries reaction rates from the subroutine where they are calculated (the oxygen routine, in this case) to the subroutine in which they are used (organic carbon). The mail trolley passes to each subroutine in the cycle, so that, for example, Mn^{2+} oxidation can contribute to the consumption of O_2 on the next pass of the cycle, without requiring the O_2 subroutine to know anything about Mn^{2+} chemistry.

[19] Convergence is based on conservation of mass to within 2% for all solid phase and dissolved constituents (appropriate balances between rain, reaction, diffusion, and burial rates). Also, the sum of the solid phase concentrations provides a convergence diagnostic. Although the solid phase dry weight fractions initially total to 1 g g^{-1}, as the computation progresses, they deviate, generally within the range of 0.5–1.5 g g^{-1}, then converge back toward a physically reasonable value of 1 g g^{-1}. Typically the model reaches convergence defined in these ways within 50–100 iterations.

[20] The coupling between solid and dissolved species in the Mn and Fe cycles was found to be too intimate to allow their separation into isolated solid and pore water subroutines. Instead, we combine the Mn species Mn^{2+}, MnO_2, and $MnCO_3$ into a manganese subroutine, and the Fe species Fe^{2+}, FeOOH, FeS, SO_4^{2-}, and HS^-, into an iron subroutine. Each subroutine returns the steady state profiles for all the solid and dissolved profiles. The residuals for all species are computed simultaneously, and cross-term derivatives such as $\partial R_{\mathrm{MnO2}}/\partial \mathrm{Mn}^{2+}$ are included in the Jacobian matrix for computing the next guess concentrations. Manganese and iron respiration are first order in organic matter and zero order in oxide above the depth of oxide depletion. Currently sulfate depletion is not expected or allowed for. $MnCO_3$ precipitation is first-order in Mn^{2+} concentration above an assumed saturation value of 150 μM, and for simplicity independent of $CO_3^=$ concentration.

[21] FeS precipitation is first order in both Fe^{2+} and S^{2-}, with a rate constant of 10^{-2} L mol^{-1} s^{-1}. Faster FeS precipitation kinetics would be more realistic but numerically intractable by these methods. Our formulation has the desired property that generally either Fe^{2+} or HS^- is dominant in pore water while the concentration of the other is low enough that diffusive transport is negligible. Therefore we expect that the steady state concentration of the major constituent, generally Fe^{2+}, will be similar to what it would be if FeS precipitation kinetics were faster. The algorithm is able to switch over smoothly from one regime to the other as the boundary conditions change.

[22] Mn^{2+} and Fe^{2+} oxidize quickly in the presence of O_2 or NO_3^-, respectively, to yield the solid oxide forms. Estimates of the Mn^{2+} lifetime in an oxic water column range from 0.9-69 days [*Wehrli et al.*, 1994] to as short as a few hours in surface sediments [*Thamdrup et al.*, 1994]. Iron oxidation lifetimes may be only a few minutes [*Sung and Morgan*, 1980]. When we incorporated oxidation reactions into the residuals for dissolved and oxide forms of Mn and Fe, we found that the relaxation method does not converge unless the oxidation kinetics were slowed unacceptably. Instead, we adopted the following simplification. The concentration of dissolved metal within the oxic zone can be approximated by the equation

$$\frac{\partial m}{\partial t} = 0 = D\frac{\partial^2 m}{\partial z^2} - \lambda m, \tag{9}$$

where D is a depth-independent diffusion coefficient and λ is a time constant for metal oxidation. The analytical solution to this

equation is an exponential dropoff of the concentration m with height above the oxic boundary z_{oxic}.

$$m(z) = m_{z_{oxic}} e^{-\sqrt{\frac{\lambda}{D}}(z_{oxic}-z)}, \quad (10)$$

where $m_{z_{oxic}}$ is the concentration of m at the oxic boundary z_{oxic}. The total rate of m oxidation can be calculated by integrating

$$\sum \text{oxidation} = \int_{z_{oxic}}^{-\infty} \lambda m dz = \sqrt{D\lambda} m_{z_{oxic}}. \quad (11)$$

Since both D and λ are known at the outset, $m_{z_{oxic}}$ can be determined by balancing the oxidation sink (or equivalently diffusion to the overlying water) against net production. Determining $m_{z_{oxic}}$ therefore completely specifies the concentration profile of m throughout the oxic zone.

[23] Our scheme, which allows us to solve for fast oxidation kinetics, replaces the full treatment of transport and reaction in the calculation of the residuals for dissolved Mn^{2+} and Fe^{2+} (as in (4)) with simple relaxation toward the concentration m

$$R_{Mn_i^{2+}} = Mn_i^{2+} - m_i. \quad (12)$$

3. Tuning to Field Data

[24] Various uncertain model parameters, such as kinetic rate constants, were tuned to optimize the fit to a 53-site data set compiled by *Morford* [1999], listed in Table 2. A plot of overlying water oxygen concentration versus the rain of organic matter in Figure 1 serves as a cross-reference between the data listing in Table 2 and the model comparison plots presented below. The total flux of organic carbon is estimated from sediment respiration rates, or based on flux chambers or oxygen microelectrode profiles corrected for organic carbon burial. Overlying water $[O_2]$ were taken from the *Levitus et al.* [1993] annual mean data set when necessary. Overlying water $[NO_3^-]$ were estimated from an empirical correlation of deep water GEOSECS NO_3^- to O_2 concentrations (Figure 2a), and clay accumulation rates were estimated from correlation with organic carbon rain in the data set (Figure 2b).

[25] The model was ground-truthed and tuned to these data using sediment rain rates (most importantly, organic carbon) and overlying water chemistry (most importantly, oxygen) as driving conditions. Model and data concentrations of organic carbon, Mn^{2+}, Fe^{2+}, NH_4^+, HS^-, the total (labile plus refractory) particulate Mn were compared at 12 cm depth, along with sediment surface Mn and the depth of NO_3^- penetration. These comparisons were each normalized to the variance of the data and model output, and combined into a cost function which we used to evaluate the overall model fit to data. Details of the cost function are given in Appendix A.

[26] Rate constants for biologically mediated processes such as organic carbon respiration and bioturbation have been shown to covary in the natural world with water depth [*Middelburg et al.*, 1997], sedimentation rate [*Boudreau*, 1994; *Tromp et al.*, 1995], and organic carbon rain [*Emerson*, 1985]. Organic carbon deposition is the energy source for benthic metabolism and is a straightforward number to extract from ocean carbon cycle models. Therefore we based the parameterizations of biologically mediated kinetics on the organic carbon rain rate.

[27] The rate of bioturbation at the sediment surface D_{B_0} was parameterized as a function of sediment accumulation rain by *Boudreau* [1994]. We converted his parameterization to one based on organic carbon rain using the empirical relation between carbon and sedimentation from *Tromp et al.* [1995], resulting in

$$D_{B_0}\left[\frac{cm^2}{yr}\right] = 0.0232\left(\text{Rain}_{\text{OrgC}}\left[\frac{\mu mol}{cm^2 yr}\right]\right)^{0.85}. \quad (13)$$

We attenuate the bioturbation rate with depth (from *Martin and Sayles* [1990]) and with overlying water oxygen concentration, as

$$D_B = D_{B0} e^{-\left(\frac{z}{z_{mix}}\right)^2} \frac{[O_{2_{BW}}]}{[O_{2_{BW}} + 20\mu M]}, \quad (14)$$

where the depth scale for bioturbation z_{mix} is taken to be 8 cm [*Martin and Sayles*, 1990] and the final factor attenuates bioturbation in low-oxygen conditions, with a half saturation constant of 20 μM O_2.

[28] The rate of pore water irrigation is based on comparisons of diffusive (microelectrode) and total (chamber) oxygen fluxes across the sediment water interface [*Archer and Devol*, 1992; *Glud et al.*, 1994; *Reimers et al.*, 1992] (Figure 3). In these locations O_2 penetrates only a few millimeters into the sediments, so the excess O_2 flux measured by the chamber is assumed to consist of an exchange of bottom water with anoxic pore water. Irrigation intensity correlates nicely with organic carbon rain, with the possible exception of low-O_2 environments; three out of four locations where $O_2 < 30$ μM showed anomalously high irrigation intensity. We parameterized irrigation intensity as

$$I_0 = 11\left[\frac{\text{a tan}\left(5\frac{\text{Rain}_{oc}-400}{400}\right)}{\pi} + 0.5\right] - 0.9 + 20\frac{O_{2_{BW}}}{O_{2_{BW}}+10} e^{\left(\frac{-O_{2_{BW}}}{10}\right)} \frac{\text{Rain}_{oc}}{\text{Rain}_{oc}+30}, \quad (15)$$

where the first two terms of the right-hand side generalizes the high O_2 conditions (solid line, Figure 3a), and the third term modifies the high O_2 result for low O_2 conditions (Figure 3b). The depth distribution of irrigation is assumed to follow a functional form

$$I(z) = I_0 e^{-\left(\frac{z}{z_{irrig}}\right)^2} \quad (16)$$

with the depth scale z_{irrig} selected by the tuner to be 1.8 ± 1 cm (Table 3). This value is shallower than the 4 cm depth scale implied by ^{222}Rn measurements [*Smethie et al.*, 1981] and used in a model of the Danish sites [*Wang and van Cappellen*, 1996].

[29] Organic carbon respiration is complicated by a range of organic carbon reactivities and by various electron acceptors. Model fits to data are improved when the organic carbon is divided into fractions with different reactivities [*Berner*, 1980]. In a steady state model the salient impact of the degradation lifetime is the depth of organic carbon reaction. Fast degradation confines carbon to the sediment surface, while slower kinetics allow mixing to distribute carbon to deeper levels, where its effect on pore water chemistry will be stronger [*Emerson and Bender*, 1981]. The depth distribution of oxic respiration can be estimated directly from oxygen microelectrode data and appears to be consistent across a range of organic carbon rain rates (B. Hales, personal communication, 1999). Hales finds that oxygen profiles from a range of locations can be fit with a double exponential, with two thirds consumed on a depth scale of a few millimeters and the rest over ~4 cm [*Hales and Emerson*, 1996, 1997; *Hammond et al.*, 1995]. We find that the best fit for the carbon rain (as opposed to oxidation) requires 50 ± 5% reactive carbon, consistent with Hales if most of the carbon burial comes from the less labile carbon fraction. Using the bioturbation rate constants calculated as above, we calculate the oxic organic carbon degradation rate constants as

$$k_j = \frac{D_{B_0}}{z^2_{\text{scale}_j}}, \quad (17)$$

where $z_{\text{scale }j}$ is the inferred O_2 consumption scale depth from Hales, using the sediment surface value of D_B. As the organic carbon rain increases, so does D_{B_0} and therefore so does k_j

Table 2. Field Data and Model Comparison[a]

Name	Reference[b]	Number	Depth	O_2	Rain	Mn^{2+}		Fe^{2+}		NH_4		OrgC		MnO_2 (8 cm)		MnO_2 (0 cm)		ZNO_3	
						Model	Data	Model	Data	Model	Data	Model	Data	Model	Data	Model	Data	Model	Data
BS1	1	1	52	211	800	0.1	13	0	1	444.9	51	2.6	2	15.4	110	29.6	440	0.3	n.d.
BS2	1	2	62	213	205	259.7	11	85.3	1	27.9	80	1.8	2	398.8	154	2193	2640	0.8	n.d.
BS3	1	3	77	75	100	115.1	19	27.7	9	12.3	50	1.9	2	1564	242	3170	484	0.7	n.d.
BS4	1	4	130	5	50	0	2	11.2	0	23.6	105	3.1	2	181.7	110	193.7	660	0.1	n.d.
BS5	1	5	181	0	25	0	n.d.	0	n.d.	31.8	100	3.5	3	192.7	60	167.6	60	0	n.d.
BS6	1	6	396	0	40	0	n.d.	0	n.d.	85.9	130	4.1	3	144.8	60	126.7	60	0	n.d.
BS7	1	7	1176	0	50	0	n.d.	0	n.d.	149.5	200	4.3	5	126.8	60	111.5	60	0	n.d.
BS8	1	8	2045	0	50	0	n.d.	0	n.d.	164.9	n.d.	4.8	5	94.2	60	81.5	60	0	n.d.
CM-CD	2	9	1443	37	28	8.6	5	2.5	n.d.	0.4	16	1.7	2.4	599.6	n.d.	783.7	n.d.	1.9	1.1
CM-CG	2	10	3320	120	64	19.6	5	4.9	40	2.1	75	1.5	2.6	908.7	n.d.	1238	n.d.	1.7	1.7
CM-CK	2	11	1000	20	37	5.9	12	1.2	1	0.4	9	1.3	0.4	673.7	n.d.	803.7	n.d.	2.7	0.5
CM-CL	2	12	1880	72	43	15	3	4	5	1.1	5	1.7	1.5	845	n.d.	1120	n.d.	1.7	1.5
CM-CM	2	13	3720	129	63	10.4	8	2.6	10	1.6	35	1.2	2.7	808.4	n.d.	1032	n.d.	1.9	2
CM-NMd	1,10	14	3111	100	17	0.3	n.d.	0.1	n.d.	0	n.d.	0.4	1.4	750.3	n.d.	708	n.d.	6.4	5
CM-NNs	1,10	15	2712	80	38	5	n.d.	1.2	n.d.	0.5	n.d.	1.1	2	707.9	n.d.	823.4	n.d.	2.3	1
DS4	3	16	190	231	905	69.3	30	154.8	140	451.9	200	1.7	4	211.6	110	2109	330	0.3	0.5
DS6	3	17	380	231	673	459	20	127.2	80	197	175	1.6	4	1600	110	8153	330	0.4	1
DS9	3	18	695	248	566	57.3	400	13.3	0	46.9	80	0.8	4	1922	200	2941	16500	1.5	1
J10BC	4	19	5036	250	18	0	0	0	n.d.	0	1	0.1	n.d.	675.6	n.d.	623.1	n.d.	100	100
J12BC	4	20	3860	240	22	0.1	0	0	n.d.	0	4	0.2	0.3	466.4	n.d.	439.6	n.d.	13.5	100
J13BC	4	21	4900	225	14	0	0	0	n.d.	0	1	0.1	0.5	712	n.d.	651	n.d.	100	100
J14BC	4	22	5100	250	11	0	0	0	n.d.	0	1	0.1	n.d.	780.3	n.d.	708.9	n.d.	100	100
J15BC	4	23	5360	250	11	0	0	0	n.d.	0	2	0.1	n.d.	800.4	n.d.	726	n.d.	100	100
J1BC	4	24	1445	240	64	20.6	6	5.7	36	0.8	41	0.8	3.3	330.7	150	438.6	320	2.9	3.5
J2BC	4	25	3000	200	30	0.7	13	0.1	n.d.	0	n.d.	0.3	0.3	431.3	780	426	1240	6.3	7.5
J3BC	4	26	2981	230	38	1.1	23	0.2	25	0.1	30	0.4	n.d.	457.3	250	458.7	1270	5.3	4.5
J4BC	4	27	1006	140	33	1.6	5	0.3	32	0.1	9	0.5	0.7	396.8	n.d.	416.1	n.d.	4.3	6
J6BC	4	28	4400	240	22	0.1	0	0	2	0	1	0.2	0.6	548.4	n.d.	514.4	n.d.	13.4	100
J7BC	4	29	4600	250	20	0	0	0	n.d.	0	4	0.1	n.d.	589.6	n.d.	550.1	n.d.	21.6	100
J8BC	4	30	2760	240	28	0.4	0	0	n.d.	0	2	0.3	0.3	409.6	n.d.	396.1	n.d.	8.5	100
Maine1	5	31	47	300	433	24.4	75	5.4	n.d.	16.4	110	0.5	1	1028	n.d.	1294	n.d.	2.8	1
Maine4	5	32	158	240	433	50.1	40	11.5	n.d.	29.6	80	0.8	1	1482	n.d.	2302	n.d.	1.6	5
Maine5	5	33	185	200	433	212.9	25	50.3	5	89.2	100	1.6	1	3014	n.d.	6798	n.d.	0.4	0.5
Maine7	5	34	290	180	433	248.8	160	58.6	n.d.	97.4	60	1.6	1	3086	n.d.	7374	n.d.	0.4	9
Maine9	5	35	250	200	433	206.3	25	48.9	2	87.4	50	1.5	1	2944	n.d.	6614	n.d.	0.5	0.5

Table 2. (continued)

Name	Reference[b]	Number	Depth	O_2	Rain	Mn^{2+}		Fe^{2+}		NH_4		OrgC		MnO_2 (8 cm)		MnO_2 (0 cm)		ZNO_3	
						Model	Data	Model	Data	Model	Data	Model	Data	Model	Data	Model	Data	Model	Data
ManopC	6	36	4450	167	20	0.3	4	0	n.d.	0	1	0.3	0.2	689.1	n.d.	650.3	n.d.	8.4	100
ManopM	6	37	3100	110	15	0.2	12	0	0	0	1	0.3	1.3	343.8	n.d.	327.3	n.d.	8.8	15
ManopS	6	38	4925	167	2	0	1	0	n.d.	0	1	0.1	0.6	832.4	n.d.	778.6	n.d.	100	100
NEP-2	7	39	3570	140	36	1.9	10	0.4	n.d.	0.2	n.d.	0.7	2	610.4	n.d.	633.2	n.d.	3.6	100
NEP-3	7	40	4211	154	33	1.2	8	0.3	n.d.	0.1	n.d.	0.5	0.8	649	n.d.	647.6	n.d.	4.3	18
NEP-4	7	41	4772	155	8	0	0	0	n.d.	0	n.d.	0.1	0.3	823.6	n.d.	752.1	n.d.	100	100
NEP-5	7	42	4980	158	5	0	0	0	n.d.	0	n.d.	0.1	0.2	828.4	n.d.	763.9	n.d.	100	100
NEP-6	7	43	5668	164	2	0	0	0	n.d.	0	n.d.	0.1	0.1	829.3	n.d.	779.4	n.d.	100	100
OMEXB	7	44	500	208	64	15	n.d.	3.7	n.d.	0.9	10	0.8	0.4	362.3	n.d.	472.9	n.d.	2.7	100
PEsc	8	45	3500	140	80	18.4	55	4.2	5	3	n.d.	1.3	1.2	863.2	989	1199	11425	1.6	4
SCB	8	46	1800	60	80	46.9	20	11.1	10	6.9	n.d.	1.9	3	1412	494	2505	6482	0.9	2
SCruz	8	47	2000	10	80	0	6	0.6	30	64.1	n.d.	5	5	284.4	385	264.5	3955	0.1	0.5
SMB	8	48	2000	5	80	0	5	15.8	150	5.6	n.d.	2.9	5	305.6	373	267.2	216	1.5	0.5
StNick	8	49	2000	35	80	81.6	30	21.7	5	9.7	n.d.	2.4	5	206.6	439	4324	28289	0.8	0.5
WEC203	9	50	1994	56	59	16.4	9	3.7	10	2.4	60	1.5	2.4	950.1	390	1397	1030	1.4	4
WEC204	9	51	110	104	246	192	8	77.7	2	75.7	63	1.8	1.5	172.4	390	3526	370	0.4	0.6
WEC206	9	52	1025	38	33	3.2	5	0.6	1	0.4	5	1	1.6	719.8	370	785.6	510	2.2	1
WEC213	9	53	620	39	48	19.5	45	4.7	5	1.8	40	1.9	2.1	990.9	360	1505	400	1.4	1.5

[a] Units for Mn^{2+}, Fe^{2+}, and NH_4^+ are μM, OrgC is in percent dry weight, MnO_2 is in ppm, and ZNO_3 is nitrate penetration depth in cm; n.d. stands for no data.

[b] References are as follows: 1, *Jorgensen et al.* [2001], *Weber et al.* [2001], and *Thamdrup et al.* [2000]; 2, *Reimers et al.* [1992]; 3, *Canfield et al.* [1993a, 1993b]; 4, *Jahnke et al.* [1989], *Lu and Emerson* [1987], R. A. Jahnke (personal communication. 2002), and *Morford and Emerson* [1999]; 5, *Christensen* [1989]; 6, *Jahnke et al.* [1982], *Klinkhammer et al.* [1982], *Emerson et al.* [1984], *Kalhorn and Emerson* [1984], *Emerson et al.* [1980], and *Reimers et al.* [1984]; 7, *Murray and Kuivila* [1990]; 8, *Shaw* [1988] and *Shaw et al.* [1990]; 9, *Hartnett* [1998], *Lambourn et al.* [1996], and *Morford and Emerson* [1999]; 10, *Lyle et al.* [1992]; and *Levitus et al.* [1993].

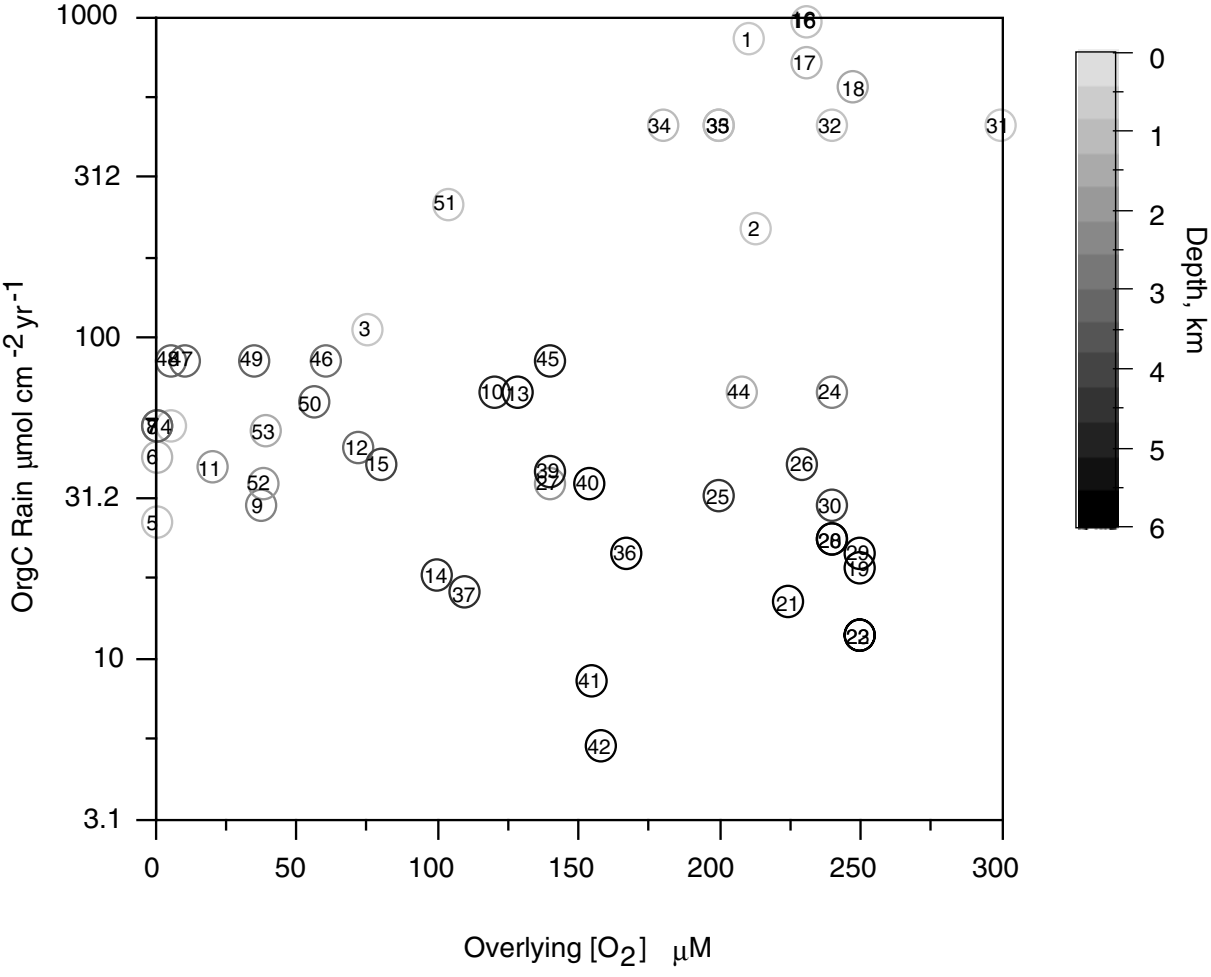

Figure 1. Overlying water [O_2] and organic carbon rain rates of the sedimentary locations in Table 2. Each location is plotted as the site number from Table 2, to enable cross-correlation with the data values in Figure 7.

(Figure 4). Note that the decrease in D_B with depth, and transport by burial, will distort the distribution of organic carbon relative to (16).

[30] The reaction rates of the two organic carbon fractions with other electron acceptors are proportional to their reactivities with oxygen. Therefore a specification of the reaction rate of slow organic carbon with some electron acceptor determines the reaction rates of the fast fraction, as for example,

$$k_{\mathrm{NO3_{fast}}} = k_{\mathrm{NO3_{slow}}} \frac{k_{\mathrm{O2_{fast}}}}{k_{\mathrm{O2_{slow}}}}. \quad (18)$$

The rate constants for denitrification were selected by the tuner to be about an order of magnitude slower than the corresponding oxic degradation rates (Table 3). The zero-order rate constants for Mn, Fe, and S respiration were derived from *Toth and Lehrman* [1977] as

$$k_{\mathrm{intermed}}\left[\mathrm{s}^{-1}\right] = 1.0753 \times 10^{-16} \alpha \left(\mathrm{Rain_{OrgC}} \left[\frac{\mu\mathrm{mol}}{\mathrm{cm}^2\mathrm{yr}} \right] \right)^{1.75}, \quad (19)$$

where a is a tunable parameter for each respiration reaction (Mn, Fe, or S). Fast and slow organic carbon reaction rate constants are derived analogously to equation (3). The best fit values of a for Mn, Fe, and S respiration rates were 1.9, 0.4, and 1.3, relative to the implicit *Toth and Lehrman* [1977] value of 1.0 (Table 3). It is interesting to note that the rate constants for oxic respiration exceeds those for alternate electron acceptors by 2–4 orders of magnitude (Figure 4), insuring that organic matter preservation will depend on overlying water oxygen concentration.

[31] As long as some nonzero concentration of organic carbon remains at depth, the pore water profiles of anaerobic decomposition products such as NH_4^+ and Fe^{2+} depend on the depth of the model domain. To eliminate this model dependence, we introduced an *e*-folding depth for respiration, a single scale depth governing all respiration reactions. The rate of oxic carbon degradation at some depth z is then taken to be

$$k_z = k\, e^{-z/z_{\mathrm{resp.scale}}}, \quad (20)$$

where k is the value at the sediment surface, calculated as described above. The model best fit used a scale depth of 3.5 ± 1.4 cm, on the shallow side of in situ measurements, which indicate 4–6 cm depth scales [*Canfield et al.*, 1993a, 1993b; *Jorgensen et al.*, 2001]. Estimates of sulfur respiration rates from deep in Deep Sea Drilling Program (DSDP) cores are orders of magnitude slower than sediment surface values, consistent with attenuation with depth as we have constructed it here [*Canfield*, 1991]. It is not clear why bacterial metabolic rates should decrease with depth in surface sediments, but whatever the reason, this dropoff appears to have a major effect on the preservation of organic matter in sediments.

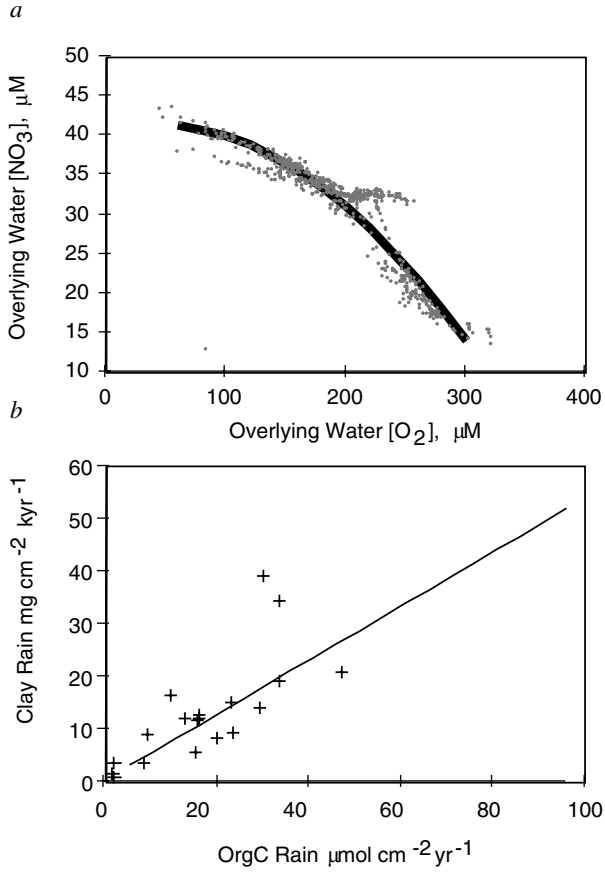

Figure 2. Further parameterizations. (a) Overlying water NO_3^- as a function of overlying water O_2, based on data from GEOSECS. Data are fit as $NO_3^- = -0.0004\ O_2^2 + 0.03\ O_2 + 41$. (b) Clay rain (accumulation) rate from the data locations in Table 2 plotted against organic carbon rain. Clay rain (mg cm^{-2} yr^{-1}) = Org Rain (μmol cm^{-2} yr^{-1})/2. [*Hartnett*, 1998; *Jahnke et al.*, 1989; *Reimers et al.*, 1992].

[32] The model is sensitive to the rain rates of reactive MnO_2 and FeOOH. We take the total rain rates of Mn and Fe to be the crustal abundance [*Turekian and Wedepohl*, 1961] multiplied by 50% bioavailability for Mn [*Nameroff*, 1996; *Shaw et al.*, 1990] and 30% for Fe [*Raiswell and Canfield*, 1988; *Raiswell et al.*, 1994]. Of these, we have greater confidence for Mn; the fraction of labile Fe depends on laboratory technique. Both variables are probably spatially variable in the ocean, but we lack the information to resolve this. Oxidation of Mn^{2+} followed first-order kinetics with a mean lifetime of about 16 min. Precipitation of $MnCO_3$ followed a first-order rate law, against a Mn^{2+} saturation concentration of 150 μ*M* with a rate constant of 10^{-10} s^{-1}.

[33] We minimized the cost function using a simulated annealing method [*Press et al.*, 1986], the strength of which is finding global minima in a complicated cost function terrain, i.e., with many local minima and maxima. Details and a discussion of the uncertainties in the tunable parameters are given in the Appendix A.

4. Results

[34] Depth distributions of pore water and solid phase chemistry are compared between model and data in Figure 5. The Patten Escarpment is a deep, high respiration but well-oxygenated site; the San Nicolas Basin is similar but with lower overlying water oxygen content [*Shaw et al.*, 1990]. The model does a reasonable job of capturing the depth dependence of the pore water data (Figure 5), but it underestimates the vertical gradients of MnO_2 at these and other sites.

[35] Model results are compared with the full data set in Figure 6. The smooth grayscale fields on the left-hand sides of Figure 6 are the model sensitivity to overlying water $[O_2]$ (10–300 μ*M* in steps of 3) and the rain of organic carbon (1–100 μmol cm^{-2} yr^{-1} in steps of 1). Biologically mediated rate constants, overlying water NO_3^-, and clay rain rates are parameterized as functions of organic carbon rain as described above. The smooth fields show the systematic dependence of organic carbon, NO_3^-, NH_4^+, Mn^{2+}, MnO_2, and Fe^{2+} on overlying water oxygen and organic carbon rain. Superimposed on the smooth model fields are data values plotted as circles. The data are located on the plot according to their overlying water O_2 and organic carbon rain rate (Table 2).

[36] Model estimates are directly compared with data on the right-hand side of Figure 6. Each comparison on the plot is numbered according to the same site numbering system used in Table 2 and Figure 3. The 1:1 lines in most cases seem to bisect the model/data points (meaning that the model is not biased). The model skill is best for organic carbon. The depth of NO_3^- penetration is quite good for most sites, but in some locations

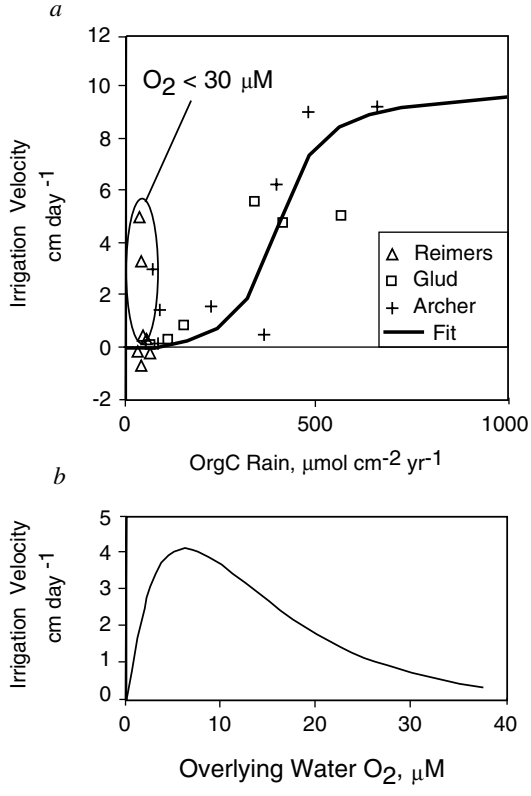

Figure 3. Parameterization of pore water irrigation. (a) Depth integrated irrigation rate, cm^3 pore water exchanged per cm^2 sediment area per day, or cm d^{-1}. Symbols are inferred from comparison of diffusive (microelectrode) versus total (benthic chamber) oxygen consumption rates. Solid line is the model parameterization in high-O_2 conditions (first two terms of (16)). Four points, demarked by the oval, were determined where the overlying water $[O_2]$ was lower than 30 μ*M*. Three of these had anomalously high irrigation intensities. (b) The third term in (16) is an oxygen dependent parameterization to simulate the apparent enhancement of irrigation observed in the data.

Table 3. Tunable Parameters in the Model

Parameter	Applied to	Best	Maximum	Minimum
F_{labile}	fraction of labile organic rain	0.5	−10% (MnO_2)	+10% (OrgC, MnO_2)
z_{resp}	respiration scale depth	3.5 cm	−40% (Fe, Mn, MnO_2)	+40% (MnO_2, NH_4)
z_{irrig}	pore water irrigation depth	1.8 cm	−60% (Fe, Mn, MnO_2, H_2S)	+60% (NH_4, MnO_2)
α_{NO3}	relative to oxic	0.3	−80% (MnO_2)	+60% (z_{NO3})
α_{Mn}	relative to *Toth and Lehrman* [1977] for S	1.9	−20% (MnO_2)	+10% (MnO_2, Mn^{2+})
α_{Fe}	relative to *Toth and Lehrman* [1977] for S	0.4	−10% (Fe^{2+}, NH_4^+)	+20% (Fe^{2+})
α_{SO}	relative to *Toth and Lehrman* [1977]	1.3	−40% (NH_4^+)	+60% (Fe^{2+}, H_2S)

the model predicts NO_3^- depletion by 25-75 cm that is not seen in the data.

[37] The distributions of Mn in solid and dissolved form are less well predicted. The grayscale plots suggest that some of the misfit is due to variability in the data. Model results vary smoothly as a function of overlying [O_2] and $Rain_{OC}$, while observed concentrations are not as well sorted by these variables. This may be because metal concentrations in natural pore waters are not in steady state or because of heterogeneity in metal deposition or geochemistry. The concentration of Fe^{2+} in pore waters, for example, varied by a factor of two between successive visits to the Patten Escarpment [*Shaw et al.*, 1990; *Zheng*, 1999]. In addition, however, the model is unable to generate the intensity of surface MnO_2 enrichment observed in, for example, the Patten Escarpment (Figure 5). We suspect that Mn^{2+} is released from nearby reducing sediments in the California Borderlands. This has been observed in shallow continental shelf sediments from the central California self via remineralization of sedimentary organic matter and calcium carbonate dissolution [*Johnson et al.*, 1992]. MnO_2 rain rates are calculated according to the fraction of Mn assumed in the clay flux, whereas Mn associated with $CaCO_3$ flux and organic carbon flux has been neglected. The elemental abundance of Mn in the detrital rain must also be higher than crustal at Manop sites H and M, where sediment surface MnO_2 reaches 20-50 ppt (a factor of 25–60 higher than crustal [*Turekian and Wedepohl*, 1961]).

[38] Most of the organic carbon rain reacts with oxygen throughout the conditions simulated by the model (Figure 7). Nitrate metabolism reaches a maximum at intermediate organic carbon rain; at high rain sites the nitrate reacts instead with Fe^{2+} diffusing up from below. Mn metabolism is highest at the boundary of MnO_2 depletion. In low oxygen conditions, half of the respiration may be attributed to anoxic metabolism.

[39] One of the advantages of the efficient relaxation scheme we employ in the Muds model is the possibility of applying the model to gridded global domains such as global ocean carbon cycle models. We present two complimentary approaches of capturing the global sedimentary carbon cycle, one based on a spatially resolved map of sediment respiration and another based on a new global oxygen-differentiated hypsometry of the seafloor.

[40] The spatially resolved model is based a $2° \times 2°$ gridded map of organic carbon rain to the deep seafloor generated by *Jahnke* [1996]. The area-weighted mean organic carbon rain rate to the seafloor is 22 μmol C m^{-2} yr^{-1}. Rain rates of $CaCO_3$ and opal are taken to be 1.4 and 1.0 times the molar ratio of $Rain_{OC}$. Clay rain rates are based on a gridded field generated by *Archer* [1996b] to drive a global model of $CaCO_3$ preservation. Overlying water chemistry boundary conditions (O_2, NO_3^-, total CO_2, and $\Delta CO_3^=$) were extracted from global gridded water column data sets [*Archer*, 1996a; *Levitus et al.*, 1993]. Rate constants are parameterized as a function of organic carbon rain, as above. The gridded field extends to 60° north and south and contains 7387 sedimentary grid points. The simulation takes a few hours on a 16-node linux cluster.

[41] Maps of organic carbon, $CaCO_3$, and labile MnO_2 are shown in Figure 8. The model shows an interesting contrast between Atlantic and Pacific MnO_2 concentrations but no equato-

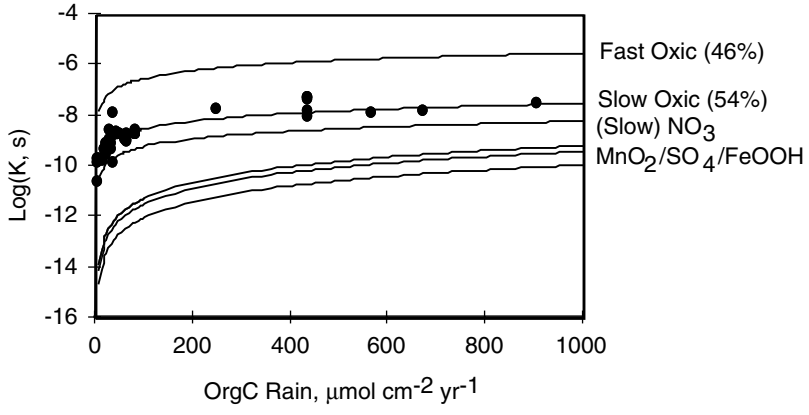

Figure 4. Rate constants for organic carbon diagenesis as a function of organic carbon rain to the seafloor. Organic carbon is split into two fractions, Fast and Slow. Oxic degradation rate constants for both fractions are compared with estimates of overall reactivity based on measured sediment organic carbon concentrations and respiration rates from Table 2. For suboxic reactions, only the Slow rates are shown; the ratio of Fast to Slow is the same as for oxic respiration.

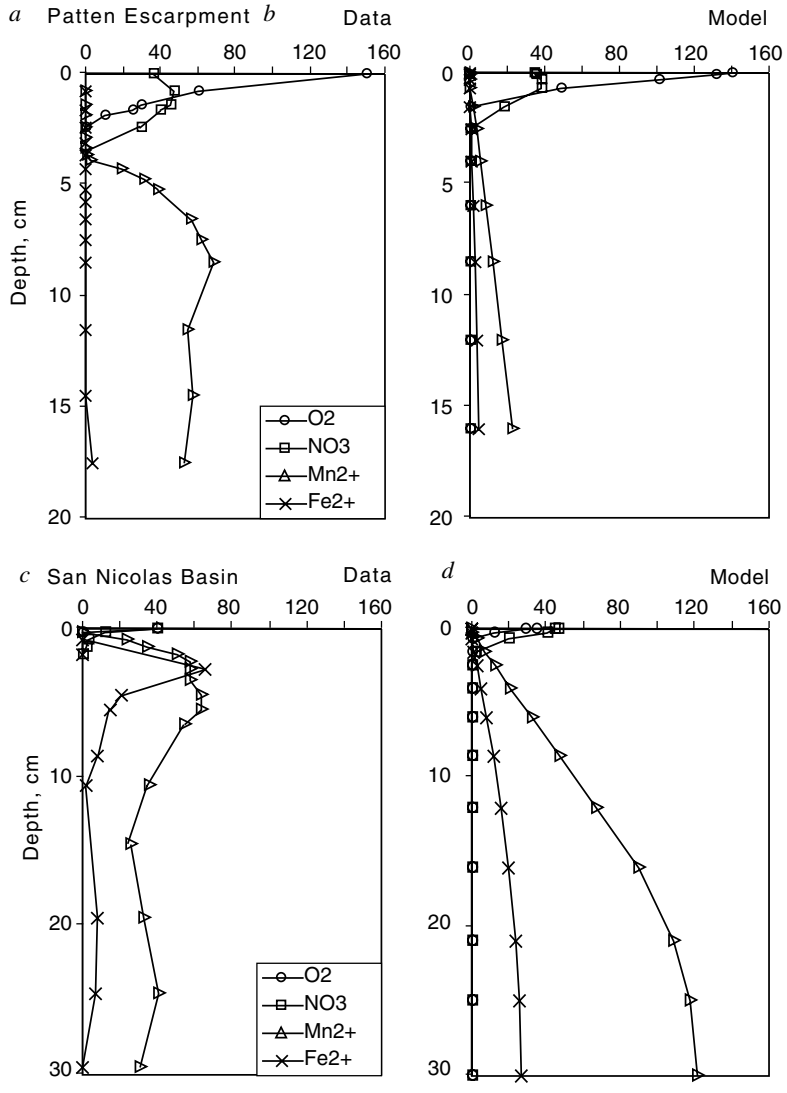

Figure 5. Pore water and solid phase chemistry comparison with data from the California Borderlands and Aarhus Bay, Denmark. (a, b, and e) Patten Escarpment and (c, d, and f) San Nicholas Basin, from *Shaw et al.* [1990]. (g and h) From station S6, Aarhus Bay, Denmark [*Canfield et al.*, 1993a, 1993b].

rial Pacific MnO_2 enrichments (Mn nodules). The carbon burial efficiency is 11%, with 94% of respiration by oxic metabolism. Organic carbon is buried at a rate of 6.0. 10^{12} mol yr^{-1}, and the total rate of denitrification is 4.3×10^{12} mol yr^{-1}. *Morford and Emerson* [1999] used the same carbon rain map and assumed oxic-only carbon degradation to calculate the area of sediments where oxygen penetrates 1 cm or less, conditions under which authigenic redox-sensitive trace metal enrichment or depletion is observed. The Muds model predicts a thin oxic zone in 3.2% of the seafloor, lower than the *Morford and Emerson* [1999] estimate of 4%, largely because of the effect of additional electron acceptors in Muds.

[42] The gridded global domain presented above is limited to locations deeper than 1000 m, excluding shallow water sediments which are generally thought to comprise 80–90% of global carbon burial [*Berner*, 1982; *Hedges and Keil*, 1995]. In an attempt to rectify this omission, we created an oxygen-differentiated hypsometry of the seafloor, depositing carbon using an empirical relationship between organic carbon rain and water depth [*Middelburg et al.*, 1997] (Figure 9a). The new hypsometry is constructed as a table of sediment area as a function of overlying water oxygen concentration and depth. These were derived from the 5° resolution ETOPO5 bathymetry, binned into the 33 depth levels of the *Levitus et al.* [1993] climatology (ranging from 10 m resolution in the upper ocean to 500 m spacing in the deep sea). For each data point in ETOPO5, we searched for the closest oxygen concentration from the Levitus annual mean field. According to our tabulation, the oxy-hypsometry of the ocean has three regions of maximum areal density (Figure 9b). Two are in the deep sea (at 150 and about 210 μM oxygen content), and a third is shallower than 100 m (ranging from 150–350 $\mu M\, O_2$).

[43] The bathymetric model predicts that 88% of the global organic carbon burial occurs shallower than 1000 m (Figure 9c). The total rate of carbon burial is 2.1×10^{14} mol yr^{-1}, a factor of 35 higher than the deep-sea based spatial model presented above. The discrepancy is due to shallow water sediments; if we restrict the bathymetric model to sediments deeper than 2500 m, the area-weighted average organic carbon rain rate, and the total carbon burial rate, is similar to the results of the spatial model results. Suboxic and anoxic respiration become more important in shallower waters, but perhaps less so than expected (sulfate respiration accounts for 15% of the global respiration in the top 1000 m,

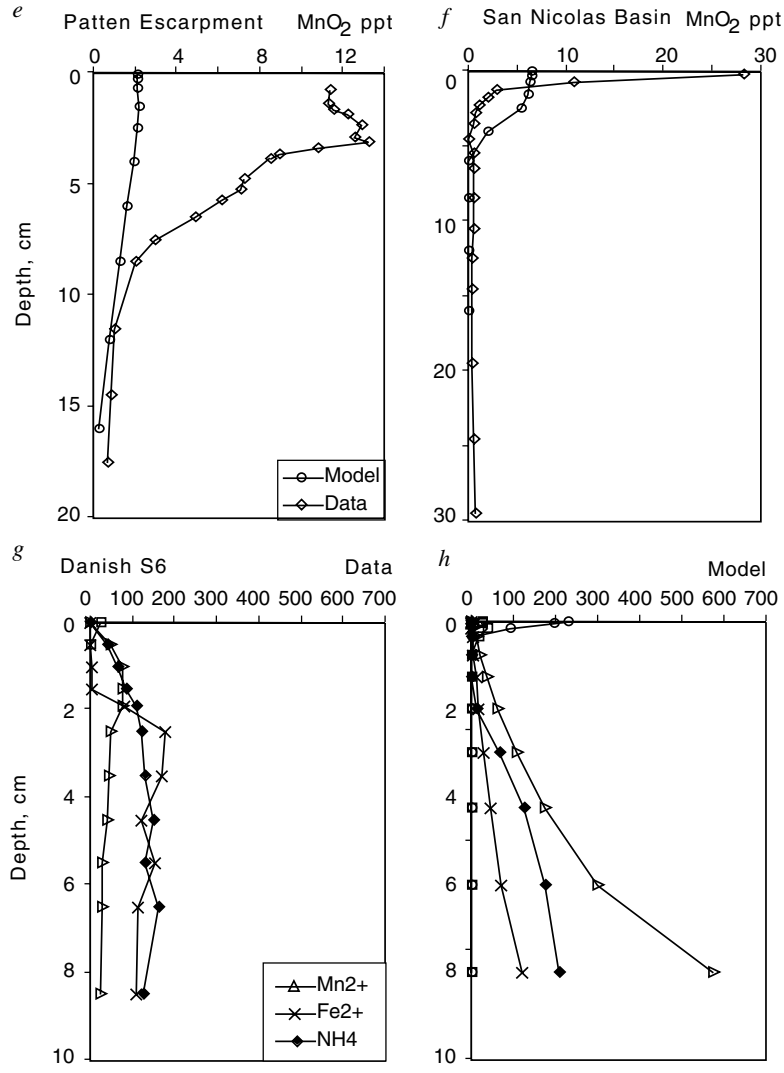

Figure 5. (continued)

compared with estimates of 35–50% from from 0 to 200 m water depth and progressively less at deeper locations [*Jorgensen*, 1982]. Overall, oxic respiration accounts for 66% of the total. Denitrification occurs primarily (88%) shallower than 1000 m, and the global rate is 1.45×10^{14} mol yr^{-1}, a factor of 33 higher than the spatially resolved model. This estimate is also a factor of 7–10 higher than the estimate of *Middelburg et al.* [1996] which was based on the same carbon rain-depth relationship. Much of the discrepancy is found in shallow waters, where the Middelberg model underestimates observed rates, and in the range of 500–1500 m, where Muds overestimates the data (Figure 10). Globally, ~30% of denitrification occurs in the depth range of 200–2000 m; if we decrease the Muds estimate by a factor of 3 in this range, the global total will be 1.16×10^{14} mol yr^{-1}, still 6–8 times higher than Middelberg, and high enough to throw the nitrogen budget of the ocean completely out of balance. Finally, the bathymetric model finds that 20.6% of the seafloor is capped with less than 1 cm of oxic sediments, a factor of 5 higher than the original *Morford and Emerson* [1999] estimate, emphasizing the importance of shallow sediments for global mass balances of redox-sensitive trace metals.

[44] In its focus on the deep sea the *Jahnke* [1996] gridded map of organic carbon rain to the seafloor resembles the output of a low-resolution ocean carbon cycle general circulation model. The comparison of gridded and bathymetric models of the global seafloor demonstrates the need to develop some parameterization of shallow-water sediments for GCM models of the ocean carbon cycle.

5. Summary

[45] We present a new model of oxic and suboxic sedimentary diagenesis which resolves the chemistry of NO_3^-, Mn, Fe, and S, and is efficient enough to incorporate into gridded global models of the seafloor. The model is tuned to solid and pore water data from a suite of 53 locations throughout the deep sea. The model does a good job of predicting the organic carbon distribution, somewhat more poorly at simulating solid phase Mn distribution. Many of the parameters are constrained to within ±50%. The model is suitable for incorporation in to heterogeneous gridded carbon cycle models, two examples of which we show here. In a gridded model of the deep seafloor, organic carbon burial efficiency is 7%, and oxygen accounts for 95% of respiration. In a global model including shallow water sediments we find that oxygen accounts for 66% overall, and that 88% of global nitrate consumption occurs in the top 1000 m.

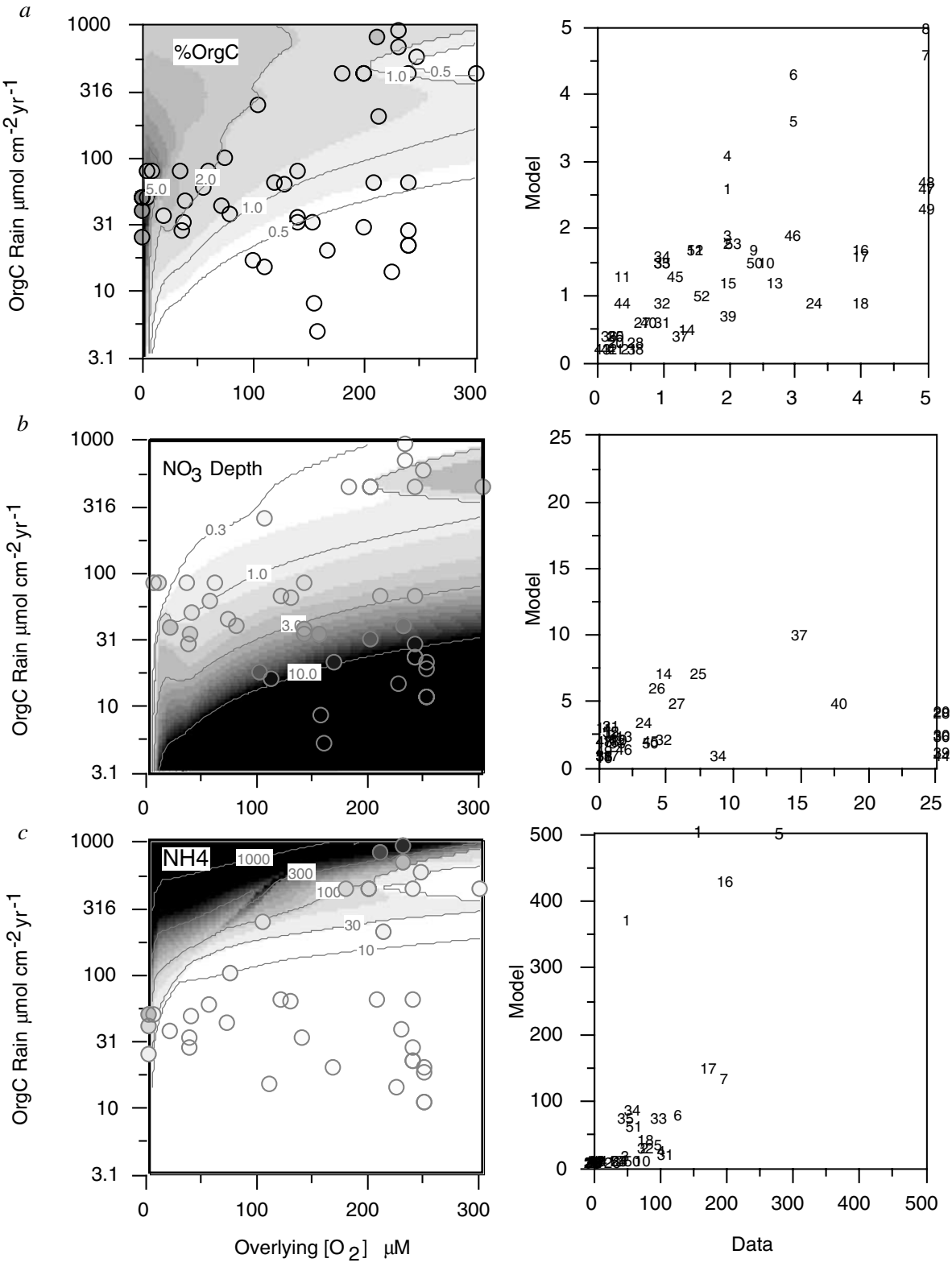

Figure 6. Model comparison with data from all sites in Table 2. Grayscale plots on the left-hand side are model fields as a function of overlying water [O_2] and organic carbon rain. Circles are data. Scatterplots on the right-hand side are a direct comparison of model and data values, indexed by site number from Table 2 and Figure 3. (a) Organic carbon at 8 cm depth (% dry weight). (b) Depth of NO_3^- penetration (cm). (c) NH_4^+ concentration at 8 cm depth, (μM). (d) Mn^{2+} concentration at 8 cm depth (μM). (e) MnO_2 concentration at the sediment surface (ppt Mn). (f) MnO_2 concentration at 8 cm depth (ppt Mn). (g) Fe^{2+} concentration at 8 cm depth (μM). (h) H_2S concentration at 8 cm depth (μM).

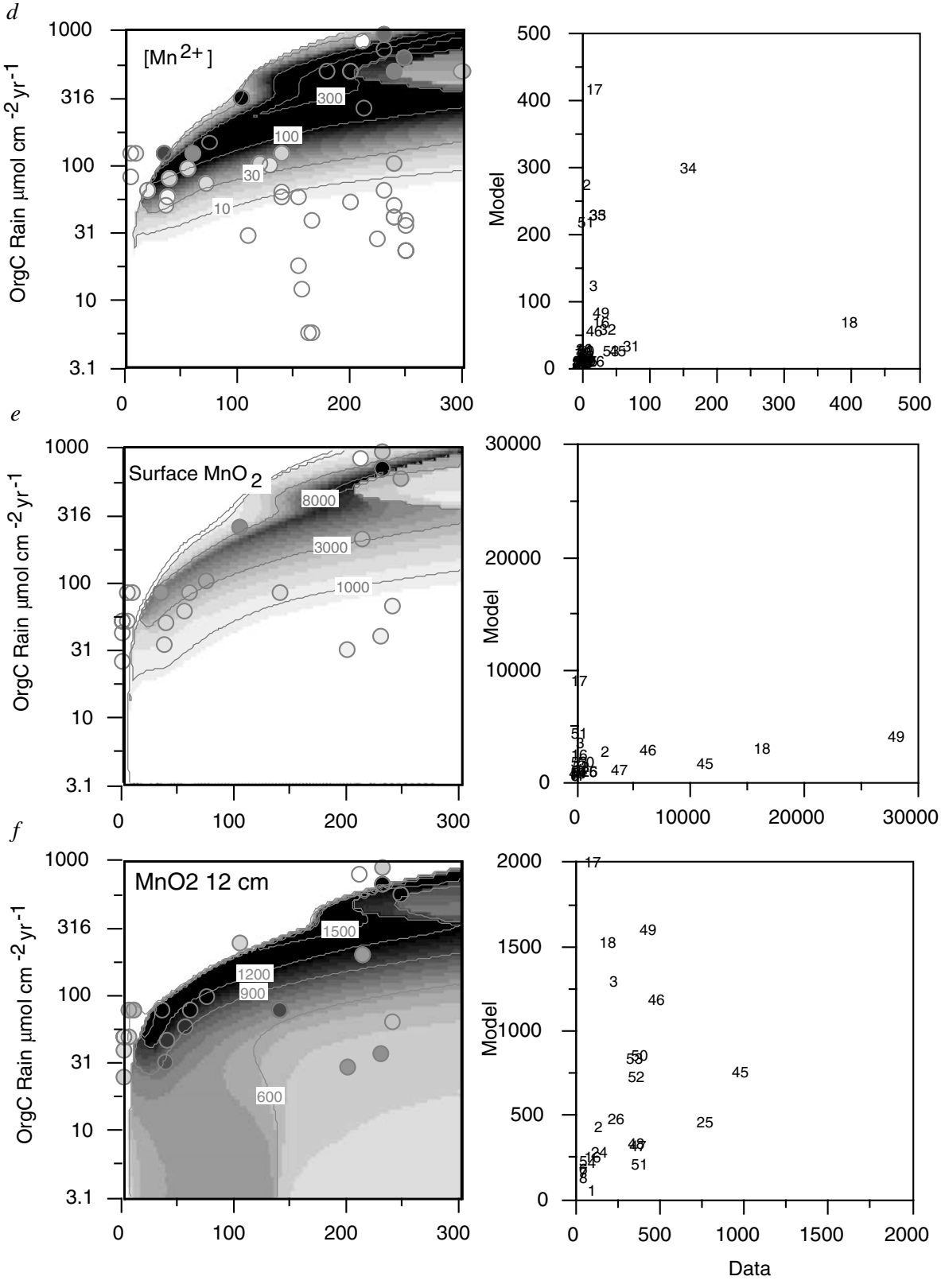

Figure 6. (continued)

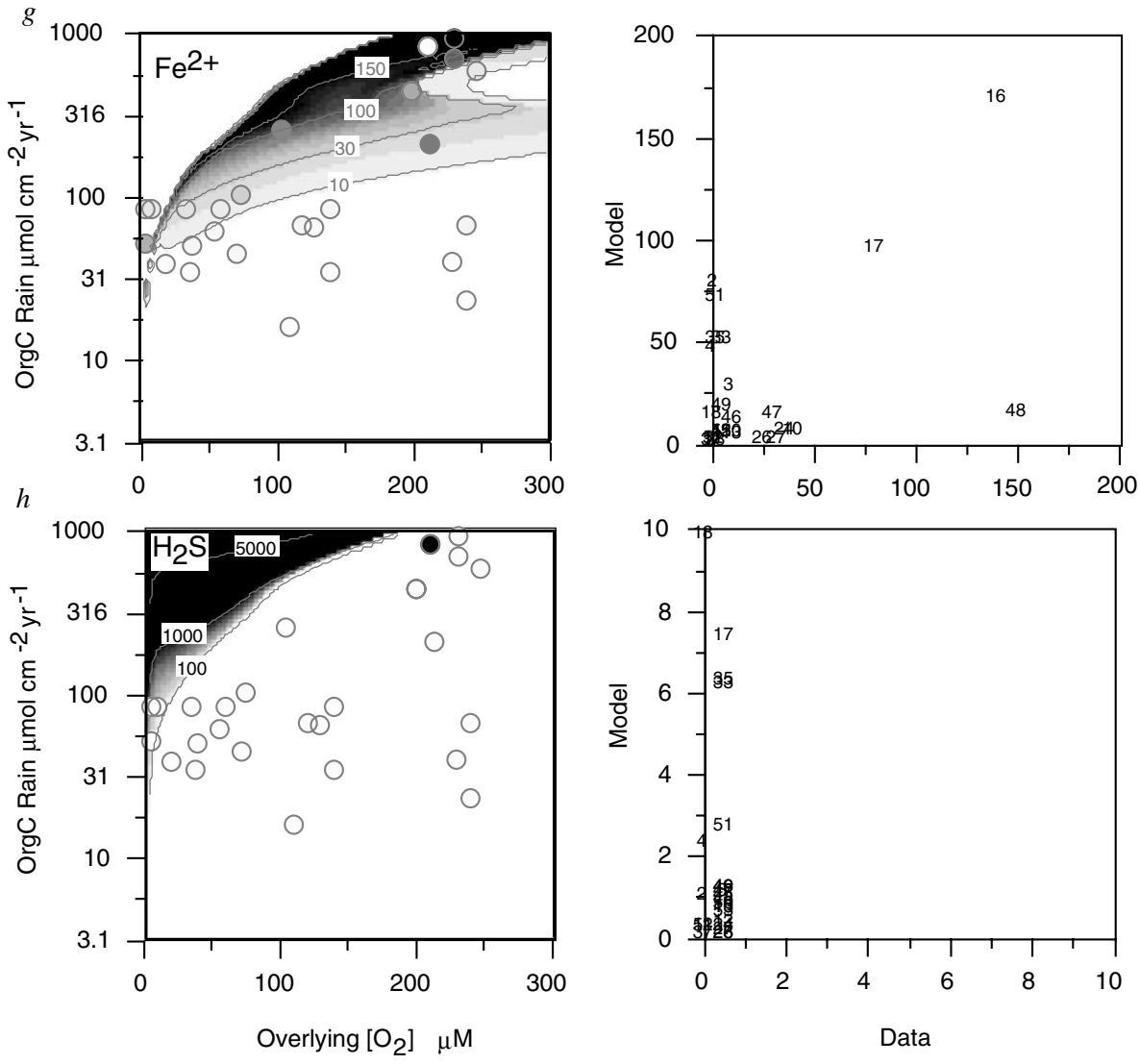

Figure 6. (continued)

[46] The Muds model can be run interactively on the World Wide Web at http://geosci.uchicago.edu/~archer/cgimodels/muds.html.

Appendix A: Automatic Tuning and Statistical Significance of the Cost Function

[47] Throughout Appendix A, subscript i denotes a data site or its model prediction, j denotes a chemical comparison, for example, organic carbon concentration, and k denotes a tuning parameter, for example, a rate constant.

[48] After considerable experimentation, a cost function was defined as

$$C_j = \sqrt{\frac{\sum_i \left(m_{ij} - d_{ij}\right)^2}{n_j}\left(\frac{1}{\sigma_{d_j}^2} + \frac{1}{\sigma_{m_j}^2}\right) + 10\left(\frac{\overline{m_j}^2 + \overline{d_j}^2}{\overline{m_j}\,\overline{d_j}} - 2\right)} + 10\sum_i \frac{\left(d_{ij} - m_{ij}\right)^2}{\left(d_{ij} + m_{ij} + \varepsilon\right)^2}. \quad \text{(A1)}$$

The cost associated with comparison j is denoted C_j, where a better fit is less costly. Data values are d_{ij}, m_{ij} is the model prediction, and n_j is the number of sites with data of type j. The first term on the right-hand side is the RMS misfit between model and data, normalized to the variance of the model and the data, $\sigma 2_{mj}{}^2$ and $\sigma_{jd}{}^2$. This term is analogous to the inverse of a correlation coefficient, with the added restriction that the data cluster around a 1:1 line. The second term strives to equate the mean values of the model and data, $\overline{m_j}$ and $\overline{d_j}$. This term served to eliminate a relative minimum near a model solution with m_j values all near zero. The third term is minimized when the ratio of each pair of d_{ij} and m_{ij} is unity, where e is a small number to prevent division by zero. This term guards against the case where a single model overestimate at one location compensates in the mean (the second term) for underestimates elsewhere. The total cost function is the sum over all chemical comparisons j

$$C_\Sigma = \sum_j C_j. \quad \text{(A2)}$$

[49] We sought optimum values of the input parameters using a simulated annealing algorithm [*Press et al.*, 1986]. The cost function was computed for an initial guess for each parameter P_k

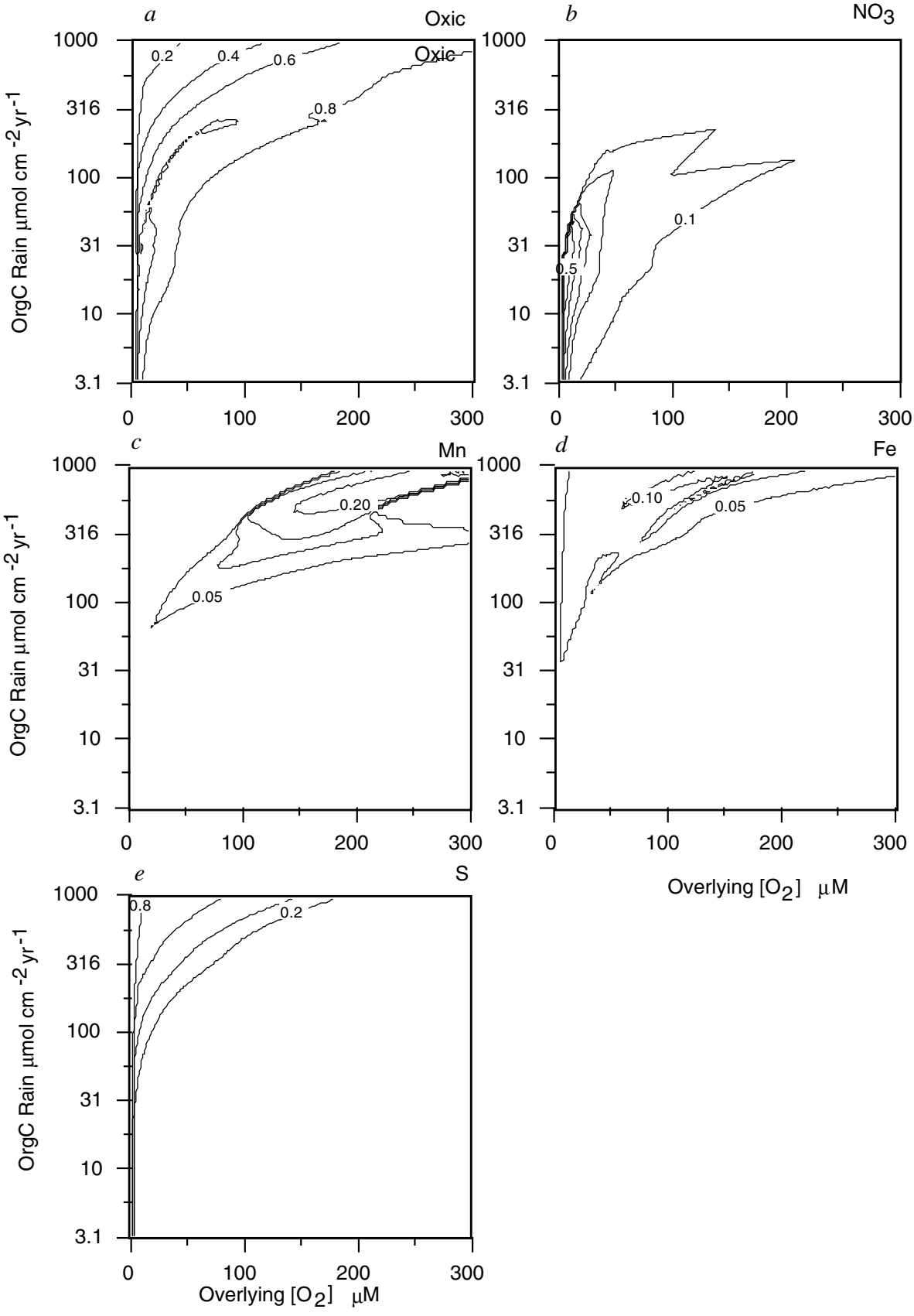

Figure 7. Fraction of organic carbon respiration due to O_2, NO_3^-, Mn, Fe, and S as a function of oxygen and carbon rain.

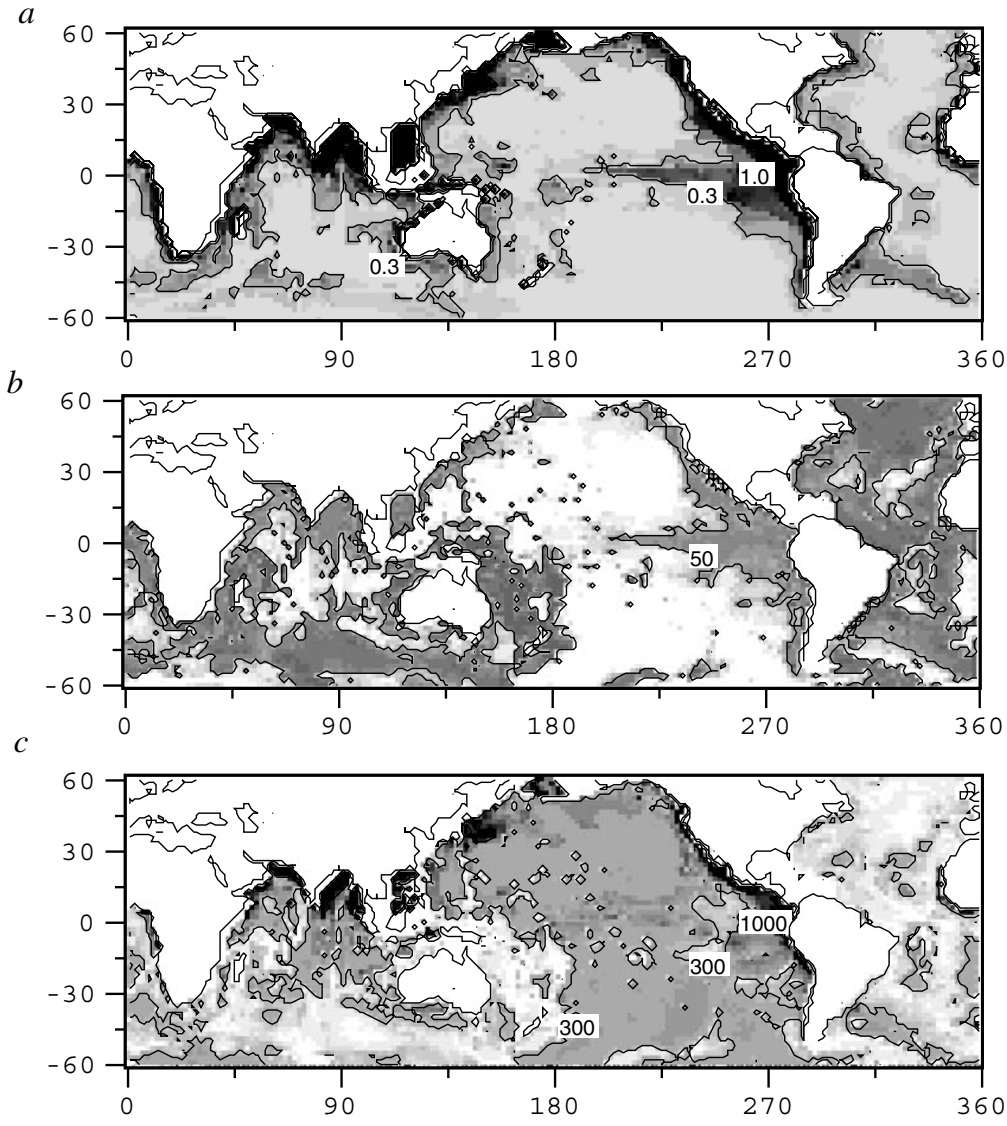

Figure 8. Global maps of (a) organic carbon (% dry weight), (b) $CaCO_3$ (% dry weight), and (c) MnO_2 (ppm dry weight) from the gridded deep-sea model run.

by running the model for each of the 53 data sites. Next, each P_k was varied randomly and independently of the others through an RMS range of ±5%. The new cost function is compared with the previous one, and the new P_k values are accepted if

$$e^{(C_{\text{init}}-C_{\text{new}}/\alpha C_{\text{init}})} > \beta, \tag{A3}$$

where β is a random number between 0 and 1 and a is temperature in the annealing analogy. In practice, if the new cost is lower than the old one, the new parameters are always chosen. If the new cost exceeds the old one, the new parameters might be chosen, with the probability governed by the temperature parameter α. The strength of simulated annealing is its ability to escape from local minima by occasionally moving uphill temporarily to higher cost functions. We also tried gradient descent method, where each parameter is tuned according to the direction of steepest descent

$$P_k^{n+1} = P_k^n - \alpha_k \frac{\partial C_\Sigma}{\partial P_k}, \tag{A4}$$

where α_k is chosen empirically to maximize stable convergence. However, we found that this method usually became trapped in local valleys, limiting its usefulness.

[50] We evaluate the uncertainties in the model input parameters by systematically varying them one at a time and recording the increase in the cost function as each parameter deviates from its best fit value. The uncertainty of an input parameter reduces to the statistical significance of the cost function; how much worse does the cost function have to be before it is considered significantly worse? As can be seen above, the cost function was formulated as a means of enforcing our subjective views of what the best fit model solution should look like. The simplest cost function, a simple RMS deviation from the data, often led to solutions in which most of the error was carried by a single tracer, NH_4, for example, which we subjectively considered an unsatisfactory solution. Hence we will treat the significance of the cost function subjectively. The results of our analysis are presented in Table 3. Most of the model parameters are constrained to within ±50% of their best fit value.

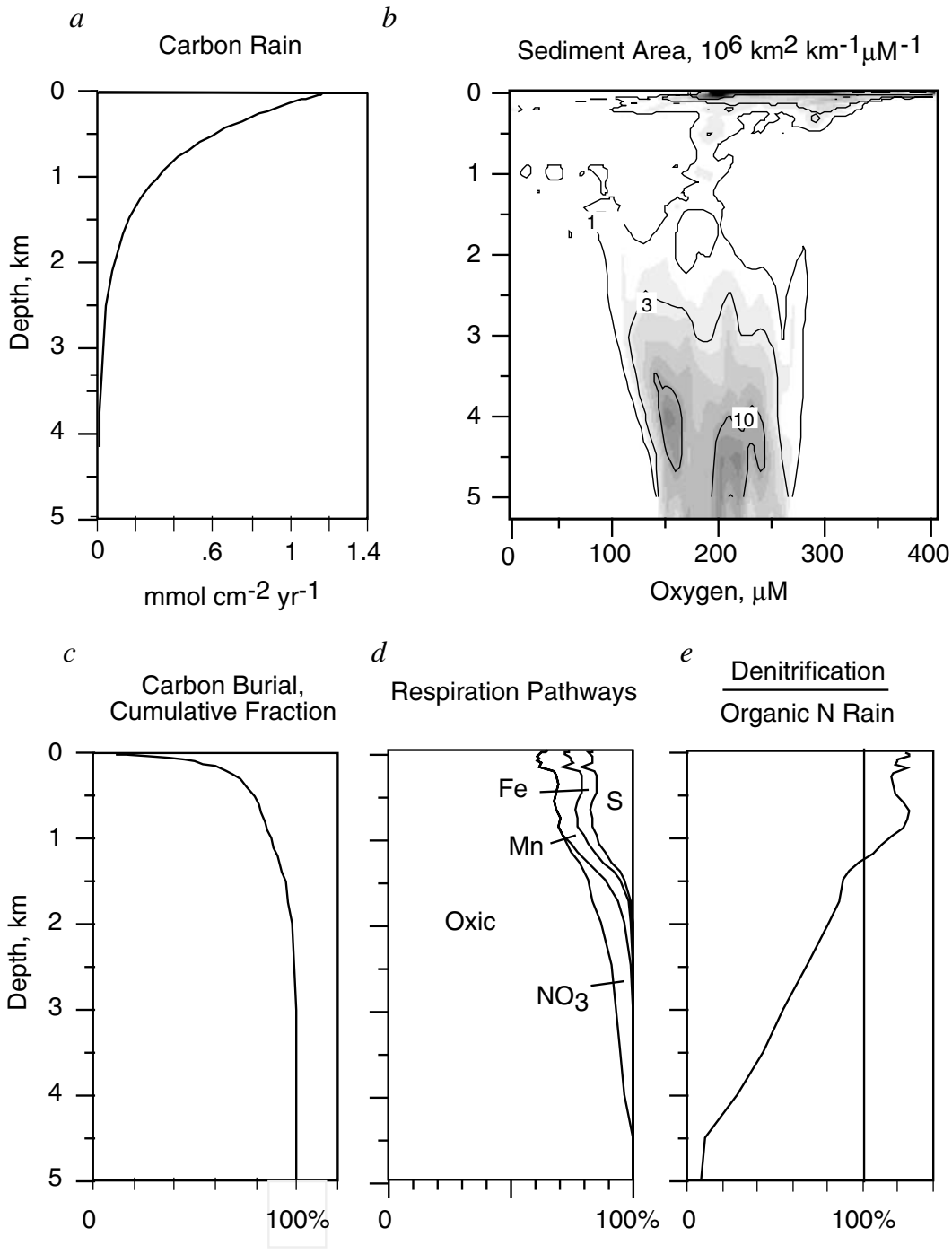

Figure 9. Global oxygen-hypsometry model of sediment respiration. (a) An average organic carbon rain rate as a function of depth, from *Middelburg et al.* [1997]. (b) A new compilation of sediment area delineated by depth (from the ETOPO5 5 min bathymetry of the ocean) and overlying water oxygen concentration (from the *Levitus et al.* [1993] annual mean gridded distribution). Units are 10^6 km^2 per km of depth interval and per μM O_2 concentration. Depth is binned into 33 ranges, corresponding to the vertical resolution of the *Levitus et al.* [1993] climatologies, and oxygen is binned into 40 bins ranging from 0 to 400 μM O_2, in increments of 10 μM. (c) Cumulative fraction of carbon burial as a function of depth in the ocean, showing that 88% of carbon buried in the model occurs shallower than 1000 m. (d) Respiration pathways as a function of depth. Shallower than 1000 m, NO_3^- is consumed by upward diffusion of Fe^{2+}, rather than by respiration reactions. (e) Ratio of sedimentary nitrate consumption to nitrogen rain to the seafloor in organic particles. In shallow waters, nitrate is extracted from overlying waters, but even here most denitrification is supported by organic nitrogen rain, consistent with *Devol* [1991]. In deeper waters, only a fraction of nitrogen rain is lost to denitrification.

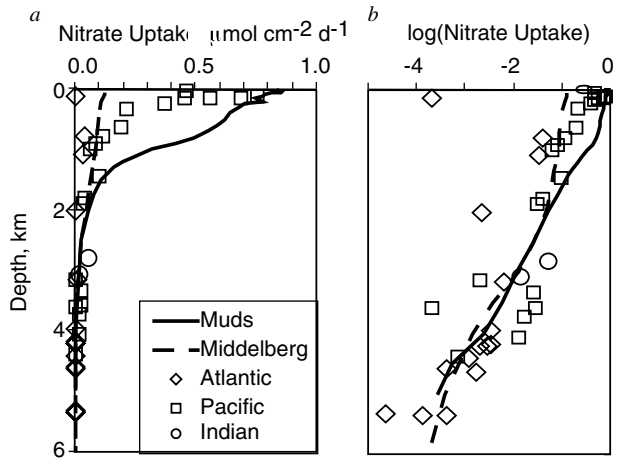

Figure 10. Comparison of sedimentary denitrification rates between Muds (solid lines), the *Middelburg et al.* [1996] model (dashed lines), and data, tabulated by *Middelburg et al.* [1996]. (a) Linear axes and (b) log axes.

[51] This analysis ignores the potential for codependence between model parameters; it could be that a simultaneous change in several parameters could still fall within the acceptable range in the cost function. Also, we are assuming that the model itself is correct, and choosing best fit values of the input parameters given that limitation. This analysis tells us more about the sensitivity of the model than about the sensitivity of the real world.

[52] **Acknowledgments.** We wish to thank Bo Thamdrup, Don Canfield, and two anonymous reviewers for helpful feedback and criticism. Jack Middelberg kindly shared data and model results. Much of this work was done while D. Archer was on sabbatical at the Danish Center for Earth System Science of the Niels Bohr Institute of the University of Copenhagen.

References

Aller, R. C., Quantifying solute distributions in the bioturbated zone of marine sediments by defining an average microenvironment, *Geochim. Cosmochim. Acta*, *44*, 1955–1966, 1980.

Anderson, R. F., et al., Late-Quaternary changes in productivity of the Southern Ocean, *J. Mar. Syst.*, *17*, 497–514, 1998.

Archer, D. E., Modeling the calcite lysocline, *J. Geophys. Res.*, *96*, 17,037–17,050, 1991.

Archer, D. E., An atlas of the distribution of calcium carbonate in sediments of the deep sea, *Global Biogeochem. Cycles*, *10*, 159–174, 1996a.

Archer, D. E., A data-driven model of the global calcite lysocline, *Global Biogeochem. Cycles*, *10*, 511–526, 1996b.

Archer, D. E., and A. Devol, Benthic oxygen fluxes on the Washington shelf and slope: A comparison of in situ microelectrode and chamber flux measurements, *Limnol. Oceanogr.*, *37*, 614–629, 1992.

Archer, D. E., and E. Maier-Reimer, Effect of deep-sea sedimentary calcite preservation on atmospheric CO_2 concentration, *Nature*, *367*, 260–264, 1994.

Archer, D., M. Lyle, K. Rodgers, and P. Froelich, What controls opal preservation in tropical deep-sea sediments?, *Paleoceanography*, *8*, 7–21, 1993.

Archer, D. E., A. Winguth, D. Lea, and N. Mahowald, What caused the glacial/interglacial atmospheric pCO_2 cycles?, *Rev. Geophys.*, *38*, 159–189, 2000.

Berger, W. H., R. C. Finkel, J. S. Killingley, and V. Marchig, Glacial-Holocene transition in deep-sea sediments: Manganese spike in the east equatorial Pacific, *Nature*, *303*, 231–233, 1983.

Berner, R. A., A rate model for organic matter decomposition during bacterial sulfate reduction in marine sediments, in *Biogeochemistry of Organic Matter at the Sediment-Water Interface*, Cent. Natl. Recherche Sci., Verrières-le-Buisson, France, 1980.

Berner, R. A., Burial of organic carbon and pyrite sulfur in the modern ocean: Its geochemical and environmental significance, *Am. J. Sci.*, *282*, 451–473, 1982.

Berner, R. A., M. R. Scott, and C. Thomlinson, Carbonate alkalinity in the pore waters on anoxic marine sediments, *Limnol. Oceanogr.*, *15*, 544–549, 1970.

Boudreau, B. P., On the equivalence of nonlocal and radial-diffusion models for porewater irrigation, *J. Mar. Res.*, *42*, 731–735, 1984.

Boudreau, B. P., Is burial velocity a master parameter for bioturbation?, *Geochim. Cosmochim. Acta*, *58*, 1243–1249, 1994.

Broecker, W. S., and G. Henderson, The sequence of events surrounding Termination II and their implications for the cause of glacial-interglacial CO_2 changes, *Paleoceanography*, *13*, 352–364, 1998.

Broecker, W. S., and T. H. Peng, The role of $CaCO_3$ compensation in the glacial to interglacial atmospheric CO_2 change, *Global Biogeochem. Cycles*, *1*, 15–29, 1987.

Burdige, D., and J. M. Geiskes, A pore water/solid phase diagenetic model for manganese in marine sediments, *Am. J. Sci.*, *283*, 29–47, 1983.

Calvert, S. E., and T. F. Padersen, Geochemistry of Recent oxic and anoxic marine sediments: Implications for the geological record, *Mar. Geol.*, *113*, 67–88, 1993.

Canfield, D. E., Sulfate reduction and oxic respiration in marine sediments: Implications for organic carbon preservation in euxinic environments, *Deep Sea Res.*, *36*, 121–138, 1989.

Canfield, D. E., Sulfate reduction in deep-sea sediments, *Am. J. Sci.*, *291*, 177–188, 1991.

Canfield, D. E., et al., Pathways of organic carbon oxidation in three continental margin sediments, *Mar. Geol.*, *113*, 27–40, 1993a.

Canfield, D. E., B. Thamdrup, and J. W. Jansen, The anaerobic degradation of organic matter in Danish coastal sediments: Iron reduction, manganese reduction, and sulfate reduction, *Geochim. Cosmochim. Acta*, *57*, 3867–3883, 1993b.

Christensen, J. P., Sulfate reduction and carbon oxidation rates in continental shelf sediments, an examination of offshelf carbon transport, *Cont. Shelf Res.*, *9*, 223–246, 1989.

Crusius, J., S. Calvert, T. Pedersen, and D. Sage, Rhenium and molybdenum enrichments in sediments as indicators of oxic, suboxic and sulfidic conditions of deposition, *Earth Planet. Sci. Lett.*, *145*, 65–78, 1996.

Dean, W., J. Gardner, and R. Anderson, Geochemical evidence for enhanced preservation of organic matter in the oxygen minimum zone of the continental margin of northern California during the late Pleistocene, *Paleoceanography*, *9*, 47–61, 1994.

Dean, W., J. V. Gardner, and D. Z. Piper, Inorganic geochemical indicators of glacial-interglacial changes in productivity and anoxia on the California continental margin, *Geochim. Cosmochim. Acta*, *61*, 4507–4518, 1997.

Devol, A. H., Bacterial oxygen uptake kinetics as related to biological processes in oxygen deficient zones of the oceans, *Deep Sea Res.*, *25*, 137–146, 1978.

Devol, A., Direct measurement of nitrogen gas fluxes from continental shelf sediments, *Nature*, *349*, 319–321, 1991.

Emerson, S., Organic carbon preservation in marine sediments, in *The Carbon Cycle and Atmospheric CO_2: Natural Variations Archean to Present*, *Geophys. Monogr. Ser.*, vol. 32, edited by A. B. Sundquist and W. S. Broecker, pp. 78–87, AGU, Washington, D. C., 1985.

Emerson, S., and M. L. Bender, Carbon fluxes at the sediment-water interface of the deep sea: Calcium carbonate preservation, *J. Mar. Res.*, *39*, 139–162, 1981.

Emerson, S., R. Jahnke, M. Bender, P. Froelich, G. Klinkhammer, C. Bowser, and G. Setlock, Early diagenesis in sediments from the eastern equatorial Pacific, I, Pore water nutrient and carbonate results, *Earth Planet. Sci. Lett.*, *49*, 57–80, 1980.

Emerson, S., R. Jahnke, and D. Heggie, Sediment-water exchange in shallow water estuarine sediments, *J. Mar. Res.*, *42*, 709–730, 1984.

Francois, R., Glacial/interglacial changes in sediment rain rate in the SW Indian sector of subantarctic waters as recorded by ^{230}Th, ^{231}Pa, U and $\delta^{15}N$ profilings in core MD84-527, *Paleoceanography*, *8*, 611–629, 1993.

Francois, R., et al., Contribution of Southern Ocean surface-water stratification to low atmospehric CO_2 concentration during the last glacial period, *Nature*, *389*, 929–936, 1998.

Glud, R. N., J. K. Gundersen, B. B. Jorgensen, N. P. Revsbech, and H. D. Schultz, Diffusive and total oxygen uptake of deep-sea sediments in the eastern South Atlantic Ocean: In situ and laboratory measurements, *Deep Sea Res.*, *41*, 1767–1788, 1994.

Hales, B., and S. Emerson, Calcite dissolution in sediment of the Ontong-Java Plateau: In situ measurements of pore water O_2 and pH, *Global Biogeochem. Cycles*, *10*, 527–541, 1996.

Hales, B., and S. Emerson, Calcite dissolution in sediments of the Ceara Rise: In situ measurements of porewater O_2, pH, and $CO_{2(aq)}$, *Geochim. Cosmochim. Acta*, *61*, 501–514, 1997.

Hammond, D. E., J. McManus, W. M. Berelson, T. E. Kilgore, and R. H. Pope, Early diagenesis of organic material in equatorial Pacific sediments: Stoichiometry and kinetics, *Deep Sea Res., Part II*, *43*, 1365–1412, 1995.

Hartnett, H., Organic carbon input, degradation and preservation in continentalmargin sediments: An assessment of the role of a strong oxygen deficient zone, Ph.D. thesis, Univ. of Wash., Seattle, 1998.

Hedges, J. I., and R. G. Keil, Sedimentary organic matter preservation: An assessment and speculative synthesis, *Mar. Chem.*, *49*, 81–115, 1995.

Jahnke, R. A., The global ocean flux of particulate organic carbon: Areal distribution and magnitude, *Global Biogeochem. Cycles*, *10*, 71–88, 1996.

Jahnke, R. A., S. R. Emerson, and J. W. Murray, A model of oxygen reduction, denitrification, and organic matter mineralization in marine sediments, *Limnol. Oceanogr.*, *27*, 610–623, 1982.

Jahnke, R. A., et al., Benthic recycling of biogenic debris in the eastern tropical Atlantic Ocean, *Geochim. Cosmochim. Acta*, *53*, 2947–2960, 1989.

Johnson, K. S., et al., Manganese flux from continental margin sediments in a transect through the oxygen minimum zone, *Science*, *257*, 1242–1244, 1992.

Jorgensen, B. B., Mineralization of organic matter in the sea bed—The role of sulphate reduction, *Nature*, *296*, 643–645, 1982.

Jorgensen, B. B., and N. P. Revsbech, Diffusive boundary layers and the oxygen uptake of sediments and detritus, *Limnol. Oceanogr.*, *30*, 111–122, 1985.

Jorgensen, B. B., A. Weber, and J. Zopfik, Sulfate reduction and anaerobic methane oxidation in Black Sea sediments, *Deep Sea Res., Part I*, *48*, 2097–2120, 2001.

Kalhorn, S., and S. R. Emerson, The oxidation state of manganese in surface sediments of the deep sea, *Geochim. Cosmochim. Acta*, *48*, 897–902, 1984.

Klinkhammer, G., D. T. Heggie, and D. W. Graham, Metal diagenesis in oxic marine sediments, *Earth Planet. Sci. Lett.*, *61*, 211–219, 1982.

Knox, F., and M. McElroy, Change in atmospheric CO_2: Influence of the marine biota at high latitude, *J. Geophys. Res.*, *89*, 4629–4637, 1984.

Lambourn, D., H. Hartnett, and A. Devol, Porewater data from the Washington shelf and slope: Cruise WE4907B of the R/V *Wecoma*, *Rep. 113*, Univ. of Wash., Seattle. 1996.

Levitus, S., M. E. Conkright, J. L. Reid, R. G. Najjar, and A. Mantyla, Distribution of nitrate, phosphate, and silicate in the world's oceans, *Prog. Oceanogr.*, *31*, 245–273, 1993.

Lu, L. G., and Emerson S. R., The carbon and nitrogen content of marine sediments from the Atlantic and Pacific Oceans, *Rep. 107*, Univ. of Wash., Seattle, 1987.

Lyle, M., et al., Paleoproductivity and carbon burial across the California current: The multitracers transect, 42°N, *Paleoceanography*, *7*, 325–333, 1992.

Mahowald, N., et al., Dust sources and deposition during the Last Glacial Maximum and current climate: A comparison of model results with paleodata from ice cores and marine sediments, *J. Geophys. Res.*, *104*, 15,895–15,916, 1999.

Martin, J. H., and S. E. Fitzwater, Iron deficiency limits photoplankton growth in the north-east Pacific subarctic, *Nature*, *331*, 341–343, 1988.

Martin, W. R., and F. L. Sayles, Seafloor diagenetic fluxes, Woods Hole Oceanogr. Inst., Woods Hole Mass, 1990.

McElroy, M. B., Marine biological controls on atmospheric CO_2 and climate, *Nature*, *30*, 328–329, 1983.

Middelburg, J. J., K. Soetaert, P. M. J. Herman, and C. H. R. Heip, Denitrification in marine sediments: A model study, *Global Biogeochem. Cycles*, *10*, 661–673, 1996.

Middelburg, J. J., K. Soetaert, and P. M. J. Herman, Empirical relations for use in global diagenetic models, *Deep Sea Res., Part I*, *44*, 327–344, 1997.

Morford, J. L., The geochemistry of redox-sensitive trace metals, Ph.D. thesis, 242 pp., Univ. of Wash., Seattle, 1999.

Morford, J. L., and S. R. Emerson, The geochemistry of redox-sensitive trace metals in sediments, *Geochim. Cosmochim. Acta*, *63*, 1735–1750, 1999.

Murray, J. W., and K. M. Kuivila, Organic matter diagenesis in the northeast Pacific: Transition from aerobic red clay to suboxic hemipelagic sediments, *Deep Sea Res.*, *37*, 59–80, 1990.

Nameroff, T., The geochemistry of redox-sensitive metals in sediments of the oxygen minimum off Mexico, Ph.D. thesis, Univ. of Wash., Seattle, 1996.

Peteet, D. M., et al., Younger Dryas climatic reversal in northeastern US? AMS ages for an old problem, *Quat. Res.*, *33*, 219–230, 1990.

Postma, D., and R. Jakobsen, Redox zonation: Equilibrium constraints onthe Fe(III)/SO_4 reduction interface, *Geochim. Cosmochim. Acta*, *17*, 3169–3175, 1996.

Press, W. H., B. P. Flannery, S. A. Teukolsky, and W. T. Vetterling, *Numerical Recipes, The Art of Scientific Computing*, Cambridge Univ. Press, New York, 1986.

Raiswell, R., and D. E. Canfield, Sources of iron for pyrite formation in marine sediments, *Am. J. Sci.*, *298*, 219–245, 1988.

Raiswell, R., D. E. Canfield, and R. A. Berner, A comparison of iron extraction methods for the determination of degree of pyritization and the recognition of iron-limited pyrite formation, *Chem. Geol.*, *111*, 101–110, 1994.

Reimers, C. E., S. Kalhorn, S. R. Emerson, and K. H. Nealson, Oxygen consumption rates in pelagic sediments from the central Pacific: First estimates from microelectrode profiles, *Geochim. Cosmochim. Acta*, *48*, 903–910, 1984.

Reimers, C. E., R. A. Jahnke, and D. C. McCorkle, Carbon fluxes and burial rates over the continental slope and rise off central California with implications for the global carbon cycle, *Global Biogeochem. Cycles*, *6*, 199–224, 1992.

Rosenthal, Y., E. Boyle, L. Labeyrie, and D. Oppo, Glacial enrichments of authigenic Cd and U in subantarctic sediments: A climate control on the elements' ocean budget?, *Paleoceanography*, *10*, 395–413, 1995.

Sarmiento, J. L., and J. C. Orr, Three-dimensional simulations of the impact of Southern Ocean nutrient depletion on atmosphereic CO_2 and ocean chemistry, *Limnol. Oceanogr.*, *36*, 1928–1950, 1991.

Sarmiento, J. L., and R. Toggweiler, A new model for the role of the oceans in determining atmospheric pCO_2, *Nature*, *308*, 621–624, 1984.

Schmitz, W., G. P. Glasby, P. Stoffers, and A. Mangini, Metal accumulation rates in sediments from the southwestern Pacific Basin, *Geochem. J.*, *33*, 79–87, 1999.

Shaw, T. J., The early diagenesis of transition metals in nearshore sediments, Ph.D. thesis, Univ. of Calif., San Diego, 1988.

Shaw, T. J., J. M. Gieskes, and R. A. Jahnke, Early diagenesis in differing depositional environments: The response of transition mdetals in pore water, *Geochim. Cosmochim. Acta*, *54*, 1233–1246, 1990.

Siegenthaler, U., and T. Wenk, Rapid atmospheric CO_2 variations and ocean circulation, *Nature*, *308*, 624–626, 1984.

Smethie, W., C. A. Nittrouer, and R. F. L. Self, The use of 222 Rn as a tracer of sediment irrigation and mixing on the Washington Continental Shelf, *Mar. Geol.*, *42*, 173–200, 1981.

Soetaert, K., P. M. J. Herman, and J. J. Middelburg, A model of early diagenetic processes from the shelf to abyssal depths, *Geochim. Cosmochim. Acta*, *60*, 1019–1040, 1996.

Sung, W., and J. J. Morgan, Kinetics and product of ferrous iron oxygenation in aqueous systems, *Environ. Sci. Technol.*, *14*, 561–568, 1980.

Thamdrup, B., R. N. Lud, and J. W. Hansen, Manganese oxidation and in situ manganese fluxes from a coastal sediment, *Geochim. Cosmochim. Acta*, *58*, 2563–2570, 1994.

Thamdrup, B., R. Rossello-Mora, and R. Amann, Microbial manganese and sulfate reduction in Black Sea shelf sediments, *Appl. Environ. Microbiol.*, *66*, 2888–2897, 2000.

Toth, D. J., and A. Lehrman, Organic matter reactivity and sedimentation rates in the ocean, *Am. J. Sci.*, *277*, 465–485, 1977.

Tromp, T. K., P. van Cappellen, and R. M. Key, A global model for the early diagenesis of organic carbon and organic phosphorus in marine sediments, *Geochim. Cosmochim. Acta*, *59*, 1259–1284, 1995.

Turekian, K. K., and K. H. Wedepohl, Distribution of the elements in some major units of the Earth's crust, *Geol. Soc. Bull.*, *72*, 175–192, 1961.

van Cappellen, P., and Y. Wang, Cycling of iron and manganese in surface sediments: A general theory for the coupled transport and reaction of carbon, oxygen, nitrogen, sulfur, iron and manganese, *Am. J. Sci.*, *296*, 197–243, 1996.

Wang, Y., and P. van Cappellen, A multicomponent reactive transport mod-

el of early diagenesis: Application to redox cycling in coastal marine sediment, *Geochim. Cosmochim. Acta*, *60*, 2993–3014, 1996.

Weber, A., W. Riess, F. Wenzhoefer, and B. B. Jorgensen, Sulfate reduction in Black Sea sediments: In situ and laboratory radiotracer measurements from the shelf to 2000 m depth, *Deep Sea Res., Part I*, *48*, 2097–2120, 2001.

Wehrli, B., G. Friedl, and A. Manceau, Reaction rates and products of manganese oxidation at the sediment-water interface, in *Aquatic Chemistry: Principles and Applications of Interfacial and Interspecies Interactions in Aquatic Systems*, edited by C. P. Huang, C. R. O'Melia, and J. J. Morgan, pp. 111–134, Am. Chem. Soc., Washington D. C., 1994.

Zheng, Y., The marine geochemistry of germanium, molybdenum, and uranium: The sinks, Ph.D. thesis, Columbia Univ., New York, 1999.

D. E. Archer, Department of Geophysical Science, University of Chicago, 5734 South Ellis Avenue, Chicago, IL 69637, USA. (archer@starbuck.uchicago.edu)

S. R. Emerson, School of Oceanography, University of Washington, Seattle, WA 98115, USA.

J. L. Morford, Woods Hole Oceanographic Institution, Woods Hole, MA 02543-1541, USA.